

Model P Wave Multipathing at Regional Distances in Southeast Asia

**Keith D. Koper
Ali Fatehi**

**Dept. of Earth and Atmospheric Sciences
St. Louis University
3642 Lindell Blvd.
St. Louis, MO 63108**

Final Report

9 June 2008

APPROVED FOR PUBLIC RELEASE; DISTRIBUTION UNLIMITED.



**AIR FORCE RESEARCH LABORATORY
Space Vehicles Directorate
29 Randolph Road
AIR FORCE MATERIEL COMMAND
Hanscom AFB, MA 01731-3010**

NOTICE AND SIGNATURE PAGE

Using Government drawings, specifications, or other data included in this document for any purpose other than Government procurement does not in any way obligate the U.S. Government. The fact that the Government formulated or supplied the drawings, specifications, or other data does not license the holder or any other person or corporation; or convey any rights or permission to manufacture, use, or sell any patented invention that may relate to them.

This report was cleared for public release and is available to the general public, including foreign nationals. Qualified requestors may obtain additional copies from the Defense Technical Information Center (DTIC) (<http://www.dtic.mil>). All others should apply to the National Technical Information Service.

AFRL-RV-HA-TR-2008-1111 HAS BEEN REVIEWED AND IS APPROVED FOR
PUBLICATION IN ACCORDANCE WITH ASSIGNED DISTRIBUTION STATEMENT.

//Signature//

ROBERT RAISTRICK
Contract Manager

//Signature//

PAUL TRACY, Acting Chief
Battlespace Surveillance Innovation Center

This report is published in the interest of scientific and technical information exchange, and its publication does not constitute the Government's approval or disapproval of its ideas or findings.

REPORT DOCUMENTATION PAGE				Form Approved OMB No. 0704-0188	
Public reporting burden for this collection of information is estimated to average 1 hour per response, including the time for reviewing instructions, searching existing data sources, gathering and maintaining the data needed, and completing and reviewing this collection of information. Send comments regarding this burden estimate or any other aspect of this collection of information, including suggestions for reducing this burden to Department of Defense, Washington Headquarters Services, Directorate for Information Operations and Reports (0704-0188), 1215 Jefferson Davis Highway, Suite 1204, Arlington, VA 22202-4302. Respondents should be aware that notwithstanding any other provision of law, no person shall be subject to any penalty for failing to comply with a collection of information if it does not display a currently valid OMB control number. PLEASE DO NOT RETURN YOUR FORM TO THE ABOVE ADDRESS.					
1. REPORT DATE (DD-MM-YYYY) 9 June 2008		2. REPORT TYPE Final Report		3. DATES COVERED (From - To) 10 Nov 2005 to 8 Aug 2008	
4. TITLE AND SUBTITLE Model P Wave Multipathing at Regional Distances in Southeast Asia				5a. CONTRACT NUMBER FA8718-06-C-0003	
				5b. GRANT NUMBER	
				5c. PROGRAM ELEMENT NUMBER 62601F	
6. AUTHOR(S) Keith D Koper and Ali Fatehi				5d. PROJECT NUMBER 1010	
				5e. TASK NUMBER SM	
				5f. WORK UNIT NUMBER A1	
7. PERFORMING ORGANIZATION NAME(S) AND ADDRESS(ES) Dept. of Earth and Atmospheric Sciences Saint Louis University 3642 Lindell Blvd. St. Louis, MO 63108				8. PERFORMING ORGANIZATION REPORT NUMBER	
9. SPONSORING / MONITORING AGENCY NAME(S) AND ADDRESS(ES) Air Force Research Laboratory 29 Randolph Rd. Hanscom AFB, MA 01731-3010				10. SPONSOR/MONITOR'S ACRONYM(S) AFRL/RVBYE	
				11. SPONSOR/MONITOR'S REPORT NUMBER(S) AFRL-RV-HA-TR-2008-1111	
12. DISTRIBUTION / AVAILABILITY STATEMENT Approved for Public Release; Distribution Unlimited.					
13. SUPPLEMENTARY NOTES					
14. ABSTRACT This report describes our analysis of seismograms recorded by the medium aperture array in Chiang Mai, Thailand (CMAR). There are two main topics covered in the report. One relates to array analysis of noise recorded over a ten year period. We document the directional characteristics of the noise as well as the seasonal variation in its amplitude. Most of this work is described in the appendix. The second topic involves array analysis of regional distance P coda waves from seismic events occurring in South Asia. Using a sliding window technique we identify coherent later arriving phases associated with the 410 km discontinuity and speculate on how their properties relate to Earth structure in the region. We also describe how the amount of near-source scattering affects coda wave amplitudes at various distances.					
15. SUBJECT TERMS Seismic characterization, Seismic propagation					
16. SECURITY CLASSIFICATION OF:			17. LIMITATION OF ABSTRACT	18. NUMBER OF PAGES	19a. NAME OF RESPONSIBLE PERSON
a. REPORT	b. ABSTRACT	c. THIS PAGE			Robert J. Raistrick
U	U	U	SAR	84	19b. TELEPHONE NUMBER (include area code) 781-377-3726

Contents

1	Executive Summary	4
2	Introduction	6
2.1	Motivation	6
2.2	Wave Propagation in the Mantle Transition Zone	7
2.3	Overview of Previous Work	9
3	Array Processing Overview	12
3.1	Description of Array Processing Techniques	12
3.2	Characteristics of CMAR	13
3.2.1	Array Geometry	13
3.2.2	Properties of the Ambient Noise Field	14
3.2.3	Signal Coherence vs. Noise Coherence	15
4	Array Analysis of CMAR Data	17
4.1	Chinese Nuclear Tests	17
4.2	Events from the NEIC Catalog (1995-2004)	18
4.2.1	Travel Time Residuals of First Arrivals	18
4.2.2	Slowness Residuals of First Arrivals	19
4.2.3	Properties of Later-Arriving Coda Waves	20
5	Conclusions and Recommendations	24
6	Acknowledgements	26
7	Figures	27
7.1	Transition Zone Ray Paths	27
7.2	Transition Zone Travel Time Curve	28
7.3	Array Response of CMAR	29
7.4	Yearly Averages of Ambient Noise at CMAR	30
7.5	Monthly Averages of Ambient Noise at CMAR	31
7.6	Hourly Averages of Ambient Noise at CMAR	32
7.7	Signal and Noise Coherence at CMAR	33
7.8	Chinese Nuclear Explosion of May 15, 1995	34
7.9	Chinese Nuclear Explosion of August 17, 1995	35
7.10	Chinese Nuclear Explosion of June 8, 1996	36
7.11	Locations of EHB Events	37

7.12	Example Beam Record Section	38
7.13	Travel Time Residuals of First Arrivals	39
7.14	Slowness Residuals of First Arrivals	40
7.15	Example Sliding Window Slowness Analysis	41
7.16	Properties of P coda at Distances Near 15°	42
7.17	P coda at Distances of $13^\circ - 18^\circ$	43
7.18	P coda at Distances of $19^\circ - 24^\circ$	44
7.19	P coda at Distances of $25^\circ - 30^\circ$	45
8	References	46
9	Appendix	50
9.1	Preprint of Koper & de Foy (2008)	50

1 Executive Summary

We carried out a synoptic study of P coda waves recorded at the medium-aperture array located in Chiang Mai, Thailand (CMAR). In particular, we focused on seismograms recorded at distances of $13^\circ - 30^\circ$ in which multiple arrivals are created by velocity discontinuities and gradients in the upper mantle. These arrivals can complicate the goals of verification seismology by, for instance, causing confusion in the identification of depth phases. Array processing techniques allow incoming energy to be sorted according to slowness, and so arrays are powerful tools in identifying the origin of later-arriving coda waves. In general, energy with vector slowness similar to the first arrival primarily comes from near-source scattering (including depth phases), energy with significantly different vector slowness primarily comes from near-receiver scattering, and energy arriving along the great circle path, but with slightly different ray parameter, is possibly related to upper mantle triplications.

To help understand the capabilities of CMAR in detecting regional distance P coda waves and resolving their slowness, we first made a thorough study of the ambient noise field. As expected from the CMAR geometry, we found that a frequency band centered near 1 Hz provided the optimal separation between signal and noise coherence. Although there were large variations from event to event, in this band correlation coefficients averaged 0.5-0.6 for signals and 0.0 for noise. This corresponds to SNR gains of about 3.2 with standard linear array processing. At frequencies below about 1.4 Hz, the ambient noise was strongly anisotropic with respect to both apparent velocity and backazimuth. Noise preferentially arrived with apparent velocities centered near 4 km/s (higher mode Rayleigh waves) and 25 km/s (teleseismic P waves), while the ring of slowness space in between (regional distance P waves) was relatively quiet. The Rayleigh noise arrived preferentially from the southwest and east, while the northerly directions corresponding to the main Asian landmass were especially quiet.

Our primary data set consisted of over 950 seismic events that occurred from 1994-2004 at distances of $13^\circ - 30^\circ$ from CMAR with continental paths in South Asia. Accurate hypocenters for these events were obtained from the EHB catalog and all the data were visually inspected and confirmed to be of high quality. We devised an algorithm that performed a sliding win-

dow slowness analysis, essentially converting the 18 time series of ground velocity recorded by the elements of CMAR into 4 times series representing beam power, beam coherence, apparent velocity, and backazimuth. We used a second algorithm to sort through the four derived time series and identify later arrivals that met specific criteria. In this way, the later arrivals were selected automatically and objectively. We also binned and stacked envelopes of beam power in order to determine average coda shapes as a function of distance.

We found that nearly all significant waves arriving within the first thirty seconds of the P wave traveled along the great circle path. This agrees with previous array-based studies of teleseismic P coda that have generally found near-source scattering to be dominant over near-receiver scattering. Near-source scattering was especially strong at distances of $27^\circ - 30^\circ$, for which it was common to observe long trains of scattering energy leading to average envelopes of beam power that were nearly flat for 30 s after the first arrival. A potential explanation for these observations is near-source scattering of R_g to P energy, perhaps by topography.

We examined various schemes for stacking array beams and in general found it difficult to make coherent images of triplicated arrivals. We attribute this to (1) the large amount of near-source scattered energy that exists at the frequencies (~ 1 Hz) for which CMAR is effective as an array, (2) the relatively small aperture (~ 10 km) and spacing of CMAR that limits its slowness resolution, and (3) regional variations in transition zone structure that cause beam stacks to become defocused. The only conclusive triplicated arrivals we observed were associated with events that occurred $14^\circ - 16^\circ$ away from CMAR in Tibet. Compared to the initial P waves these arrivals were 6-8 s later, 3-5 times larger, and had ray parameters 2-3 s/deg smaller. These properties are consistent with waves that have either dived beneath the 410 km-discontinuity or been post-critically reflected from it. The differential times are slightly larger than predictions from IASP91, which may imply a slightly deeper 410-km discontinuity beneath eastern India and Burma; however, the first arrivals have negative absolute residuals themselves and so it may be that the upper portion of the upper mantle in this area is seismically fast.

2 Introduction

2.1 Motivation

The current emphasis on detecting and locating low-yield nuclear explosions makes understanding regional distance ($13^\circ - 30^\circ$) seismic data especially important. At teleseismic distances signals are often too weak to be recorded and at local distances there are often few (or even no) accessible seismic stations. But body wave propagation at regional distances is complicated because the waves turn in the upper mantle and strongly interact with the seismic discontinuities and sharp radial gradients in the mantle transition zone (MTZ). These interactions result in the appearance of several discrete geometric arrivals, often referred to as a triplication or triplicated arrivals. Here we use the more general term of multipathing to describe this phenomenon. Although multipathing is sometimes used specifically in the context of lateral variations in velocity, we emphasize that in this study all of the interpretation and modeling assumes 1D wave propagation.

Multipathing complicates the goals of verification seismology in several ways. At certain distances the first arrival may be 5-10 times smaller than a secondary arrival. Depending on which peak is chosen, the station estimate of m_b can be significantly biased. It is also possible that a small first arrival is obscured by noise, leading an analyst to pick the larger secondary arrival as the nominal first arrival. The corresponding travel time anomaly then biases the location estimate. The existence of multiple arrivals can also lead to confusion in identifying depth phases, which are one of the most effective tools in discriminating earthquakes from explosions. Furthermore, multipathing could lead to the inference of a complicated source time function, or multiple discrete sources, when in fact only a single, simple source exists. On the other hand, if multipathing is properly recognized the differential times can lead to increased location accuracy (e.g. Ringdal, 1981).

It is well-known that the structure of the MTZ varies from region to region. A recent comprehensive study of receiver functions found that MTZ thickness varies globally by ± 35 km (Lawrence & Shearer, 2006). Thickness is defined as the difference between the depths to the 410-km and 660-km discontinuities, and is more robust than estimates of topography on either discontinuity. In addition to these two standard global discontinuities, there

is evidence for many other discontinuities that exist at least regionally and perhaps globally. These include the Lehmann discontinuity near a depth of 220 km (e.g., Dziewonski & Anderson, 1981; Karato, 1992; Gaherty & Jordan, 1995; Deuss & Woodhouse, 2004), the X-discontinuity at depths near 300 km (e.g., Revenaugh & Jordan, 1991; Ganguly & Frost, 2006), and a discontinuity near 520 km (e.g., Shearer, 1990; Ryberg et al., 1997; Deuss & Woodhouse, 2001). Furthermore, there is evidence for extreme regional variation in the velocity structure just above the 410-km discontinuity, perhaps indicative of partial melt (Revenaugh & Sipkin, 1994; Song et al., 2004). Therefore, each region of interest in verification seismology must be independently studied and in a sense calibrated if upper mantle multipathing is to be properly understood.

In this project we target the continental region of South Asia as seen by the small aperture seismic array in Chiang Mai, Thailand (CMAR). We use an array station because it allows for a large increase in signal-to-noise-ratio (SNR), especially at the high frequencies common in regional seismograms of small events. Since CMAR has been active for over ten years, this leads to a relatively large database of earthquake waveforms allowing for a synoptic study. An array station also provides the capability of using slowness analysis to separate multiply arriving waves by ray parameter, or in other words, to apply wavenumber filters to the data. While depth phases and near-source scattered waves are expected to have ray parameters close to the first arrival, multipathing created by MTZ structure is expected to produce arrivals that vary by as much as 3-4 s/deg relative to the first arrival. We also note that CMAR is located at regional or far-regional distances from several known test sites, including Lop Nor, China (24.7°); Pokhran, India (26.4°); Ras Koh, Pakistan (32.9°); and Chik-tong, North Korea (34.4°).

2.2 Wave Propagation in the Mantle Transition Zone

Example paths for rays traversing the mantle transition zone are shown in the top panel of Figure 7.1. Here we use the IASP91 velocity model (Kennett & Engdahl, 1991) and consider a range of ray parameters from 8.0 s/deg to 15.0 s/deg, equally spaced in increments of 0.05 s/deg. The head wave P_n is not naturally simulated with geometric ray tracing, however a rich variety of refractions and reflections are visible. The focusing of energy near $1^\circ - 2^\circ$ is created by postcritical reflections from the Moho (PmP) and is commonly

observed in seismograms recorded at local distances. More relevant to this study is the focusing of energy at $15^\circ - 20^\circ$ created by returns from the 410-km and 660-km discontinuities. This is also the most extreme region of multipathing, with IASP91 predicting 7 distinct arrivals (not including non-geometrical contributions to P_n) at some of these distances. Generally, by 30° the multipathing ends, however for velocity models with a strong discontinuity near 220 km, such as PREM, asthenospheric phases are predicted out to nearly 40° .

In the middle panel of Figure 7.1 we present ray paths for all the geometric P waves at 17° . IASP91 predicts 5 distinct arrivals, two associated with the low velocity asthenosphere, one turning above the 410, one reflecting off of the 410, and one diving beneath the 410. The three shallowest rays arrive within 1.3 s of one another and differ by at most 1 s/deg in ray parameter. Therefore, it would be difficult to discriminate among these arrivals, even with data from a high quality array station. This is especially true because near-source scattered energy, which often contributes to the coda, is expected to have a similar ray parameter. However, the two deeper rays arrive at ray parameters 2-3 s/deg smaller than the three shallow rays, and so even though the predicted times are somewhat close, a wavenumber filter may separate the later arrivals from coda and/or depth phases of the first group of arrivals.

The bottom panel of Figure 7.1 shows the three rays predicted by IASP91 to exist at 26° . These rays form a classic triplication of a ray turning above the discontinuity, a ray reflecting from the discontinuity, and a ray diving beneath the discontinuity. In this case the diving wave arrives first, about three seconds ahead of and 1 s/deg steeper than the shallow turning ray. The reflected ray arrives just 0.3-0.4 s behind the shallow turning ray, steeper by about 0.3 s/deg. So while it is unlikely to be possible to discriminate between the two shallower waves using an array station, it may be possible to discriminate the diving ray from the other two.

A travel time curve for regional distances is shown in Figure 7.2. The curve was created using the taup methodology of Buland & Chapman (1983) and the IASP91 velocity model. We show the curve in reduced space in which a slowness of 11 s/deg was used to offset the move-out. The cusps associated with the transition zone phases are labeled A thru F and are ordered in terms of decreasing ray parameter. The AB branch turns above the 410,

the BC branch reflects off the 410, the CD branch turns in between the 410 and the 660, the DE branch reflects off the 660, and the EF branch turns below the 660. Points E and C are predicted to have large amplitude as they represent the the angle of critical reflection for rays incident on the 410 and 660, respectively. Technically, rays reflected at precritical angles extend the curves at points C and E back towards smaller distances, however these rays are expected to have small amplitude. Likewise, diffraction is expected to extend the curves at points B and D to greater distances, but again amplitude is expected to drop off quickly, especially at short periods.

Clearly, different velocity models lead to different travel time curves. For instance, increasing the depth to the 410 km discontinuity delays the BC branch in time and shifts it to larger distances. However, for reasonable velocity models the general character of the curve is unlikely to change fundamentally, and the IASP91 predictions can be used to gain insight on the observability of transition zone phases. The most promising distance range to distinguish and identify triplicated waves in observed data is likely at $13^\circ - 15^\circ$. Here the $P_{BC/CD}$ phases are expected to arrive significantly later and less steeply than P_{AB} and shallower phases, and to have relatively large amplitude. A similar situation exists at distances of $17^\circ - 18^\circ$ for waves grazing the 660 km discontinuity. The third promising distance is around $27^\circ - 28^\circ$ near the D cusp in which $P_{CD/DE}$ rays arrive with a large time separation relative to P_{EF} , though with similar ray parameter.

2.3 Overview of Previous Work

Many previous studies have used seismic arrays to study upper mantle structure. When the first teleseismic arrays were deployed in the early 1960's, it was quickly realized that the direct observations of $dt/d\Delta$ (ray parameter) provided by arrays were superior to those obtained with the more common method of smoothing and differentiating a travel time vs. distance curve. The derivative information ($dt/d\Delta$ as a function of Δ) was necessary to obtain a radial velocity model via the Herglotz-Weichert method. One of the earliest such studies was that of Niazi & Anderson (1965). These authors used data recorded at the Tonto Forest array in Arizona to measure $dt/d\Delta$ for 70 shallow events occurring at distances of $10^\circ - 30^\circ$. They noticed abrupt changes in $dt/d\Delta$ at distances of 17° and 24° and inferred discontinuities to exist at depths of 320 km and 640 km respectively. The example seismograms

presented in Niazi & Anderson (1965) show clear later arrivals, but the authors were unable to include these observations in the modeling because of uncertainties in the depths of the sources. Presumably, the authors were worried about misinterpreting depth phases as triplicated arrivals. However, the potential value of these arrivals was recognized, with the final sentence of Niazi & Anderson (1965) stating, “Clearly, later arrivals must be used to determine details of transition zones”.

A closely related study was published two years later using a similar data set recorded at the Tonto Forest array (Johnson, 1967). In this case, the author was able to observe and model multiple transition zone arrivals, stating that “A general conclusion of this study is that later arrivals provide crucial data for eliminating much of the non-uniqueness in the velocity structure”, and reporting evidence for strong gradients (discontinuities) at 400 km and 650 km. The primary difference in the two studies was that while Niazi & Anderson (1965) used data from the standard 10 km aperture cross configuration at Tonto, Johnson (1967) used a version of Tonto augmented with 8 seismometers that yielded an effective aperture of about 300 km. Most likely, the increased ray parameter resolution provided by the increased aperture contributed to the ability of Johnson (1967) to confidently identify and model the triplicated arrivals.

A thorough study of the upper mantle beneath Australia was published in 1974 using data recorded from the Warramunga (WRA) seismic array (Simpson et al., 1974). The authors measured the ray parameter of 494 P wave arrivals from sources located at distances of $10^\circ - 30^\circ$. WRA is a medium-sized array, aperture of about 20 km, and the authors reported a precision of better than 0.1 s/deg in slowness determination. They found pronounced later arrivals at $21^\circ - 24.5^\circ$, which they associated with a discontinuity at 650 km, and large amplitude later arrivals at $12^\circ - 18^\circ$, which they associated with a discontinuity near 400 km. Even so, they commented on the non-uniqueness of the problem and avoided a direct inversion of their observations; instead they used forward modeling to determine a consistent model (SMAK I) and properly identify the later arrivals.

Similar studies involving two other medium aperture, United Kingdom style arrays were carried out over the next few years. Ram & Mereu (1977) analyzed data from over 350 earthquakes at distances of $14^\circ - 36^\circ$ from the

Gauribidanur array (GBA) in India. The authors found later arrivals and abrupt changes in $dt/d\Delta$ of the first arrivals that were consistent with discontinuities at 400 km and 650 km. They also discussed the possibility of lateral variation in MTZ structure, dividing their data set into fourths based on backazimuth and inverting for separate velocity models. Ram et al. (1978) analyzed data from over 100 earthquakes recorded at the Yellowknife Array (YKA) in Canada and found similar results, although the later arrivals were not as clearly defined. Transition zone multipathing has also been observed in data from LASA in Montana (see Figure 6 of Filson (1975)) and NORSAR in Norway (Ringdal, 1981), although we did not find any dedicated studies in the mainstream geophysical literature.

In more recent years, the trend has been to use regional seismic networks (as opposed to medium aperture arrays) to make record sections of MTZ multipathing at distances of $10^\circ - 30^\circ$ for a relatively small number (as opposed to a large number) of sources. For instance, Walck (1984) used data from ten earthquakes recorded in Southern California, to constrain MTZ structure beneath the Gulf of California; Lefevre & Helmberger (1989) modeled data from seven earthquakes recorded at seismometers across North America to infer upper mantle structure beneath the Canadian Shield; Ryberg et al. (1998) used data from approximately a dozen peaceful nuclear explosions in the former Soviet Union to image the MTZ in northern Eurasia; Zhao et al. (1999) used data from eight earthquakes recorded across a temporary seismometer network in South Africa; Song et al. (2004) modeled waveform data generated from approximately 8 earthquakes off the coast of Oregon and Washington and recorded at regional networks throughout the Western U.S.

Hence, the work described in this report is somewhat of a “retro” study, having more in common with work done in 1960’s and 1970’s when seismic arrays were relatively new. This is warranted because our primary interest is not in inferring Earth structure, but in understanding wave propagation in South Asia in the context of verification seismology. The primary challenge is that the array considered here (CMAR) was designed as a regional array, with an aperture approximately half that of the medium aperture arrays (WRA, YKA, GBA) that were successfully in the past studies of upper mantle multipathing described above. Therefore, we can expect poorer slowness resolution and potentially more difficulty in identifying later arriving phases.

3 Array Processing Overview

3.1 Description of Array Processing Techniques

The array processing software used in this study was previously developed by the PI under the acronym GAP (Generic Array Processing) (Koper, 2001) and has been slightly modified for the current project. The core problem of slowness inference is carried in the time domain by repeated beam formation over a 2D Cartesian grid of slowness vectors. The beam giving the highest mean-square power over the prescribed time window is chosen as the optimal beam, and the corresponding slowness vector is chosen as the optimal slowness vector. This technique is sometimes referred to as beampacking and is roughly the time-domain equivalent of traditional fk techniques (Schweitzer et al., 2002). We use it because it implicitly averages over frequency, while being very localized in time. Therefore, like VESPA analysis (Davies et al., 1971), it is well-suited for analyzing multiple body waves that arrive in short amount of time.

The user is required to enter a time window, corner frequencies and number of poles for a bandpass filter, a type of beam, and spacing constraints on the slowness grid. In this study we commonly use 3-pole Butterworth bandpass filters, and phase-stack weighted (PSW) beams. The PSW beams amplify coherent energy but induce less waveform distortion than n^{th} root beams (Schimmel & Paulssen, 1997). We find that this leads to more precise slowness estimates. The traces are also resampled from 0.05 s to 0.01 s to increase precision. Each array element is weighted equally during beam formation and no special allowance is made for the local noise structure. We experimented with inferring 3D slowness vectors that account for elevation differences among the array elements, but found no compelling advantages. This is expected because CMAR is relatively flat, having a maximum elevation difference of only 0.066 km, compared to a horizontal aperture of 10.1 km (see Bokermann (1995) for a discussion of topographic effects on slowness inference).

When necessary, error estimates are made using a bootstrap technique (Tichelaar & Ruff, 1989) that generates pseudo arrays by resampling the elements with replacement, repeating the grid search, and generating a population of pseudo-solutions. A covariance matrix is estimated from this pop-

ulation and then converted into a 95% confidence ellipse. Also, individual standard errors for the ray parameter and backazimuth are obtained from the population of pseudo solutions. We use this method, as opposed to computing some sort of F-statistic, because our definitions of power generally arise from non-linear beam formation techniques that are not necessarily expected to follow standard probability distributions.

We also operate the core slowness inference process in a sliding window mode. This allows for the generation of ray parameter and backazimuth time series, in addition to beam power and coherence as a function of time. Movies that show power as a function of ray parameter, backazimuth, and time can also be output. Our measure of coherence is the stack of the instantaneous phases of the aligned traces, which varies from 1 for perfect coherence to 0 for perfect incoherence (Schimmel & Paulssen, 1997). In this work, the data are generally filtered around 1.0 Hz, and we have found a window length of 2 s provides good results. The sliding window is shifted in increments of 0.2 s, giving a 90% overlap. We commonly do not obtain individual error estimates when the slowness estimation process is run in a sliding mode.

3.2 Characteristics of CMAR

3.2.1 Array Geometry

The short-period Chiang Mai array consists of 18 elements arranged in a roughly circular geometry (Figure 7.3). The resulting 153 inter-element separations range from 1.46 km to 10.07 km, reflecting a design goal of detecting relatively small magnitude, regional distance seismic events. Figure 7.3 also shows the CMAR response function (as defined by Rost & Thomas (2002)) at two representative frequencies. Owing to the circular geometry of CMAR, the ARF is very symmetric azimuthally, and can be well-approximated as a 1D function of ray parameter. At 1 Hz the half-width of the center peak is about 6 s/deg, while at 3 Hz the half-width is about 2 s/deg. In both cases, prominent sidelobes fall outside of the slowness range for regional distance P waves, and spatial aliasing is not expected to be a problem.

3.2.2 Properties of the Ambient Noise Field

We examined the ambient noise field at CMAR using data recorded during 950 randomly chosen, 4-sec long time windows. For each time window we calculated a 2D slowness grid with the horizontal components of slowness varying from -40 s/deg to 40 s/deg in increments of 0.2 s/deg. Beams were computed using phase-stack weighting on traces bandpass filtered from 0.67-1.33 Hz and resampled to 0.01 s. Each grid was then normalized by its peak amplitude before being included in a grid stack. Therefore, our technique does not recognize the absolute level of noise at a given time, but only its distribution in slowness space.

The 1-Hz, time-averaged ambient noise field at CMAR possesses three distinct, coherent peaks that are robust from year-to-year (Figures 7.4, 7.5, and 7.6). The most prominent occurs to the southwest at a backazimuth near 220 degrees and an apparent velocity of 3.5-4.0 km/s; the next largest occurs at apparent velocities above 15-16 km/s, generally from the south although backazimuth is poorly determined because of the high apparent velocities; the smallest peak occurs almost due East, with apparent velocities of 3.5-4.0 km/s. Importantly, the region of most interest in a monitoring sense, basically everything arriving from the North, is relatively quiet at most times.

These initial observations were interesting enough that we did a comprehensive study of the ambient noise at CMAR. The full analysis is described in Koper & de Foy (2008), which is attached to this report as an Appendix, and here we just mention the main results:

- At frequencies above 1.4 Hz the noise at CMAR is isotropic and diffuse.
- At frequencies lower than 1.4 Hz the noise at CMAR is strongly partitioned by apparent velocity into two categories: teleseismic P wave energy with apparent velocities higher than 25 km/s (ray parameters of 0.0-5.0 s/deg) and higher mode Rayleigh energy with apparent velocities near 4.0 km/s.
- The Rayleigh noise is further partitioned by direction, with the strongest signal arriving from the Bay of Bengal at backazimuths of 180-255°. A secondary peak in the Rayleigh noise occurs in the direction of the South China Sea at backazimuths of 80-120°.

- The Rayleigh noise is strongly seasonal with annual variations of 10-15 dB in power. For a magnitude scale such as MS(Vmax) (Russell, 2006; Bonner et al., 2006) that depends directly on the logarithm of seismic amplitude, our observations imply that the detection threshold at CMAR varies by 0.5-0.75 magnitude units according to direction and time of year.
- Like the Rayleigh noise, the P noise observed at CMAR is seasonal. It has an annual power variation of 5-10 dB and there are several geographic regions that could act as sources: the western Atlantic Ocean near the coast of northern Brazil may contribute PKP energy, the Pacific Ocean just north of New Guinea may contribute PcP energy, and central portions of the North Pacific may contribute P waves that turn in the lower mantle.

3.2.3 Signal Coherence vs. Noise Coherence

We also examined the relative coherence of signal and noise as a function of frequency and interstation spacing, using data from 950 events that occurred mainly to the northwest of CMAR (a complete description of these events is given in a later section). We used the following procedure for each event:

1. The unfiltered traces were resampled to 0.01 s and aligned on the first arrival with a standard cross-correlation algorithm.
2. One of six frequencies bands (centered on 0.2 Hz, 0.5 Hz, 1.0 Hz, 2.0 Hz, 3.0 Hz, and 4 Hz) was chosen and a narrow, 3-pole Butterworth band-pass filter was applied to each trace.
3. Correlation coefficients for the 153 distinct element pairs were computed for a 10 s window starting 2 s before the first arrival (signal), and a 10 s window starting 1 minute before the first arrival (noise).

The approximately 145,000 correlation coefficients in each frequency band (for both signal and noise time windows) were then sorted into inter-element distance bins with widths of 1 km. The means and standard deviations of each bin are shown in Figure 7.7 for the six frequency bands.

Technically, the correlation coefficients should be Z-transformed before the mean and standard deviations are computed because of the non-Gaussian

nature of the correlation coefficient distribution (van Decar & Crosson, 1990); however, this correction will not alter the fundamental features shown in Figure 7.7. We find that the frequency band giving the largest gap between signal coherency and noise coherency is centered at 1 Hz, and therefore this band should yield the highest gain during beam-formation. In this band, the noise is almost perfectly uncorrelated across the entire array, while the signal maintains an average correlation coefficient near 0.55. Using equation 6 from Mykkeltveit et al. (1983) this corresponds to an average gain of about 3.2, significantly less than the classic \sqrt{N} gain of 4.2 that would be expected if the signal were perfectly correlated. It is important to note that the preferred frequency range near 1 Hz that we infer is potentially only valid for regional distance events to the northwest of CMAR. As shown in Figures 7.4, 7.5, and 7.6, the 1 Hz noise in other geographical quadrants (and at small ray parameters in general) is often significantly coherent. Therefore, we might expect the largest gap between signal and noise coherence to be at a higher frequency band for these directions.

4 Array Analysis of CMAR Data

4.1 Chinese Nuclear Tests

We first examined data from three Chinese nuclear explosions that were recorded at CMAR. These events have relatively simple source time functions and no depth phases that could interfere with later arriving direct phases. High quality locations for these three events are given by Fisk (2002) as:

Date	Time	Lat.	Lon.	m_b	Distance	Backazimuth
1995/05/15	04:05:59.38	41.5545	88.7516	6.1	24.65	341.5
1995/08/17	00:59:59.35	41.5402	88.7533	6.0	24.64	341.5
1996/06/08	02:55:59.37	41.5780	88.6875	5.9	24.69	341.4

where distance and backazimuth are calculated relative to the beam reference point. At this distance IASP91 predicts three arrivals associated with the 660 km discontinuity. The first is an P_{EF} wave that turns beneath the 660 with a ray parameter of 9.1 s/deg; about 1.3 s later a P_{CD} arrival that turns above the 660 with a ray parameter of 10.3 s/deg is expected; and about 1.1 s later a P_{DE} wave that reflects off of the 660 with a ray parameter of 9.7 s/deg is expected.

Record sections and slant stacks for these three events are shown in Figures 7.8, 7.9, and 7.10 respectively. In each case there appears to be three peaks in slowness space that could plausibly be associated with the three expected arrivals. This is especially true for the May 15, 1995 explosion shown in Figure 7.8. It also appears that the first arrivals in each slantstack have the largest ray parameter, perhaps implying that for this path the depth to the 660 km is slightly larger than in IASP91 and so the P_{CD} phase arrives in advance of P_{EF} . However, each peak is smeared and significantly interferes with the others. Considering that these three events are essentially colocated, it is disappointing that the three slantstacks are not more similar. Partially this is due to this specific distance being near a branch intersection on the traveltime curve (Figure 7.2), however it is also indicative of the small aperture of CMAR as discussed in the introduction. More sophisticated techniques (i.e., Capon, 1969; Schmidt, 1986; Shumway et al., 2008) could

potentially provide more accurate estimates of slownesses for triplicated arrivals; however, all slowness estimators are likely to have problems when the signals arrive from similar directions at similar times (Shumway et al., 2008).

4.2 Events from the NEIC Catalog (1995-2004)

Our original data set consisted of over 1,700 events that occurred from 1995-2004 at distances of $13^\circ - 30^\circ$ from CMAR. We selected only those events that had primarily a continental path and those for which a P wave arrival at CMAR was reported in the NEIC. As we began processing these data we noticed that many had large travel time residuals relative to IASP91, and in some cases the nominal arrival time reported in the NEIC catalog did not match a noticeable feature in the data. Therefore, in order to improve the overall quality of the data set we decided to cull events with poor quality locations.

To classify which events to keep and which to eliminate we consulted the updated EHB catalog of re-processed ISC locations (Engdahl et al., 1998). We accepted those events from our original data set for which (1) the *isol* field was HEQ, DEQ, or FEQ, (2) there was no x in the *iseq* field, and (3) the *ahyp* field was not Z. This reduced our data set to 955 events, but led to a more consistent and high quality data set. We then replaced the original NEIC hypocenters with the EHB hypocenters. The distribution and statistics of this data set are shown in Figure 7.11. It is complete down to a magnitude of about $4.7 m_b$. Most of the seismicity forms an arcuate belt representative of the ongoing collision between India and Eurasia. Also, most of the seismicity is shallow, with the main exception being intermediate depth events in the Hindu-Kush zone in Afghanistan. An example record section of array beams is shown in Figure 7.12.

4.2.1 Travel Time Residuals of First Arrivals

For each event we visually inspected the traces and eliminated those that had glitches, null segments, or electronic noise. We then filtered the data using a 3-pole Butterworth bandpass with corners of 0.67 Hz and 1.33 Hz, formed linear beams using the expected slowness vector, and hand picked the arrival

times of the first arriving waves. This was partially done for quality control, but also because these times were needed to align beams prior to stacking them in bins of distance or azimuth. Our initial processing indicated that theoretical times, even for EHB locations, were not accurate enough to produce coherent beam stacks.

The corresponding travel time residuals are shown geographically, and averaged in bins of distance, in Figure 7.13. The distribution is nearly Gaussian with a mean of -0.11 s and a standard deviation of 1.64 s. We attribute the remarkably small bias to the high-quality of the EHB locations and the appropriateness of IASP91 as an average velocity model for the region. Coherent geographical patterns appear in the residuals, such as the patch of near-zero values for events in Pakistan and the strongly negative signal for events in Tibet; however, it's unclear if these patterns are related to true 3D variations in geology or simply reflect an inaccuracy in the 1D reference model (note the distance dependence to the travel time residuals). Obviously, data from many more stations and earthquakes would be required to generate the crossing paths required for a tomographic study.

4.2.2 Slowness Residuals of First Arrivals

A previous study of slowness anomalies at CMAR caused by near receiver heterogeneities found a median ray parameter residual of -1.35 ± 0.58 s/deg and a median backazimuth residual of $7.3 \pm 12.4^\circ$ (Bondar et al., 1999). This level of inaccuracy is large enough to cause confusion among various upper mantle branches of the travel time curve, especially near cusps (Figure 7.2). However, those authors also found that the slowness anomalies depended significantly on incoming direction and the values reported above are an average over all regions of slowness space. Therefore, as a further check on data quality, but more importantly to assess the accuracy of CMAR-based slowness estimates for regional distance events from the northwest, we estimated 2D slowness vectors for all of the first arrivals in our data set.

We filtered the data with a 3-pole Butterworth bandpass, using corner frequencies of 0.67 Hz and 1.33 Hz, and determined the optimal slowness vector for each event by doing a grid search over beam power in Cartesian slowness coordinates. The beams were calculated using third order phase

stack weighting and power was measured over a 4 s window that started 1 s before the picked first arrival time. In Figure 7.14 we show the resulting residuals assuming EHB locations and the IASP91 velocity model. We find mean residuals of -0.84 ± 1.14 s/deg and -0.28 ± 1.16 s/deg for East/West and North/South slowness respectively. The trend is remarkably constant for various incoming directions and therefore is probably created by some sort of geological heterogeneity near the array. In general though, the ray parameter estimates are only mildly biased, with a mean residual of 0.18 ± 1.26 s/deg. The observed ray parameters nicely track the expected change of about 5 s/deg as distance increases from 13° to 30° . This implies that measured ray parameters for later arrivals, at least near cusps C and E, should be distinguishable from the first arrival ray parameters.

4.2.3 Properties of Later-Arriving Coda Waves

We experimented with several approaches in an effort to make images of coherent later arriving phases. For instance, we tried stacking vespagrams that had been formed at theoretical backazimuths into bins according to distance, and we tried coherent and incoherent stacking of array beams for specific source regions. In general though, these efforts were unsuccessful and we ultimately settled on a technique that simply identified significant later arrivals on an event-by-event basis. We then binned these arrivals by distance and looked for trends in slowness, timing, and relative amplitude.

Our technique for identifying significant later arrivals is described as follows. For each event we performed a sliding window slowness analysis, starting 10 s prior to the picked first arrival time and continuing for 40 s. The windows were two seconds long and were shifted in increments of 0.2 s, giving a 90% overlap. Optimal slowness vectors were determined for each window using a grid-search method similar to what was described in the previous section and with the same frequency band. For each event, this resulted in four time series with equal lengths of 201 points: beam power, coherence, ray parameter, and backazimuth. Example output for this procedure is shown in Figure 7.15.

We then tested several criteria for identifying significant arrivals from these time series. The following requirements led to a nice balance between

not generating too many spurious arrivals while not missing legitimate but small-amplitude arrivals. First, we multiplied the linear beam power by the square of the coherence and applied two passes of a nearest-neighbor smoothing filter. Any local maximum on this curve was then accepted as an arrival if it had (1) a signal-to-noise ratio of at least 5 on the original linear beam, (2) a coherence of at least 0.8, and (3) a ray parameter estimate less than 16 s/deg. For the event shown in Figure 7.15, which is typical, this procedure resulted in seven distinct arrivals as shown by the red stars. Modest changes in our acceptance criteria led to small or no changes in the number of significant arrivals.

Results from this procedure are shown in Figure 7.16 for a group of shallow events (depth less than 40 km) that occurred at distances of $14.5^\circ - 15.5^\circ$. The amplitude of each later arrival is scaled according to the event-specific maximum and then plotted as a function of ray parameter, backazimuth, and lapse time. There is some scatter in the backazimuth estimates but they clearly cluster around the value for the first arrival. This is true even for the very small amplitude arrivals that are only 10%-20% as large as the maximum. We also found this to be true for the other distance ranges in our data set. This implies that most of the P -coda we observe is created by near-source heterogeneity and multipathing. While some near-receiver $P - R_g$ scattering may occur, there appears to be very little near-receiver $P - P$ scattering.

From the stack of normalized beam power time series shown in Figure 7.16, it is clear that there are two distinct pulses of energy for events occurring at distances around 15° . As shown in the upper right panel, the secondary energy arrives about 6-8 s after the first arrival and has ray parameters 2-3 s/deg smaller than the first arrival. These properties are consistent with P_{BC} arrivals that have reflected off of the 410-km discontinuity and/or P_{CD} arrivals that have turned beneath the 410-km discontinuity. It is the drop in ray parameter in particular that distinguishes these arrivals from pP_{AB} depth phases. As a numerical example, consider a 40 km deep event occurring at 15° from CMAR (such deep crustal events are relatively common in Tibet). The following arrivals are predicted by IASP91:

Phase	Travel Time (s)	Ray Parameter (s/deg)
P (AB)	-	13.1
P (asth.)	0.20	13.6
P (asth.)	0.35	13.5
P (CD)	4.87	11.1
P (BC)	4.97	11.2
pP (AB)	8.00	13.6
pP (asth.)	8.26	13.3
pP (asth.)	8.28	13.5
pP (CD)	14.72	11.1
pP (BC)	14.74	11.2

So, while depth phases from shallow P waves could plausibly explain the observed differential times, they cannot explain the observed drop in ray parameter. Furthermore, synthetic seismograms show that interfering $P_{BC/CD}$ waves near the C cusp often have bigger amplitudes than the first-arriving P_{AB} wave. Finally, we point out that these strong later arrivals show up at distances out to 18° , but at progressively smaller differential times (Figure 7.17). This is the expected behavior for P_{CD} arrivals, but not for pP_{AB} depth phases.

The mean differential time between the largest arrival and first arrival for the 15° distance bin is 6.9 ± 1.7 s (after removing 4 outliers). This is about 2 s larger than predictions from IASP91 for a surface focus, implying either that P_{AB} is too fast, $P_{BC/CD}$ is too slow, or some combination of the two. We previously found evidence that P_{AB} waves (the first arrivals) are fast for this area (Figure 7.13); in fact, the mean absolute P_{AB} residual for these events is about -2 s. So the simplest explanation is that the uppermost mantle beneath Burma is seismically fast, perhaps due to extra thick lithosphere or lid, while the region around the 410 km is nicely described by IASP91. Alternatively, some of the anomaly in P_{AB} - $P_{BC/CD}$ differential times could be caused by a slightly depressed 410 km discontinuity in the region. A depression of 10 km would add about 0.5 s to the differential time. Given this level of non-uniqueness, formal modeling of Earth structure is not warranted.

In Figure 7.18 we show depictions of significant later arrivals for distances of $19^\circ - 24^\circ$. The $P_{DE/EF}$ branch of arrivals is expected to appear 5-6 s after the first arrival with significantly reduced ray parameter, but there is no

compelling trend in the observations. This may be related to the sparseness of data at distances of $22^\circ - 24^\circ$ and is not necessarily an indicator of non-standard structure near the 660 km discontinuity. At the largest distances of $25^\circ - 30^\circ$ (Figure 7.19) we again see evidence of multipathing in the upper mantle. Especially at distances of $27^\circ - 29^\circ$ secondary arrivals appear 2-6 s after the first arrival with significantly increased ray parameter, as predicted for P_{DE} arrivals. However, there is wide variation in the differential times and ray parameters, and no strong constraints can be placed on Earth structure.

It is worth noting that at the largest distances of $28^\circ - 30^\circ$ the stacked beam power envelopes flatten out considerably, with many strong arrivals occupying the entire time window of 30 s after the first arrivals (Figure 7.19). Only shallow events (depth < 40 km) are included in these stacks, and so it cannot be that the arrivals are depth phases from intermediate depth earthquakes in the Hindu-Kush seismogenic zone. Instead, the nearly flat coda envelopes are likely indicative of increased near source scattering. A plausible (though non-unique) explanation of this energy is scattering of R_g to P from topographic features in the source region. The relatively slow velocity of R_g provides a mechanism for generating significant P energy far after the first arrival with only a single scattering event. Evidence exists for such a mechanism based on nuclear explosion data from Nevada Test Site (Stead & Helmberger, 1988; Gupta et al., 1991). However, for this mechanism to be viable the earthquakes in this area would have to be especially shallow, as R_g excitation drops off significantly with increasing source depth.

5 Conclusions and Recommendations

Using the medium-aperture array in Chiang Mai, Thailand we studied the properties of P coda waves for a group of 955 events that occurred at distances of $13^\circ - 30^\circ$. We found that nearly all coherent energy in the first 30 s after the P wave arrives along the great circle path. This indicates that near receiver scattering, which would generally lead to large slowness anomalies, contributes very little to the coda waves. Nearly all coherent energy also arrives with ray parameters within 2-3 s/deg of the first arrival. The majority of this energy seems to be associated with near-source scattering, perhaps R_g into P , though this would require especially shallow earthquakes.

Although we were unable to produce to images of transition zone multipathing with various beam-stacking techniques, we did observe clear evidence for upper mantle multipathing from events occurring in Tibet at distances of $14^\circ - 17^\circ$ from CMAR. We observed secondary arrivals associated with ray paths that either dive beneath the 410 km discontinuity (P_{CD}) or reflect off of it (P_{BC}), that had anomalously large differential times relative to the first arriving P_{AB} phase. The differential times were too large by about 2 s which is nearly equal to the absolute P_{AB} residuals determined from EHB locations. Therefore, while a depressed 410 km discontinuity may contribute to the anomalous differential travel times, it is more likely that the shallow mantle beneath Burma is anomalously fast, perhaps because of a thickened lid.

In general, the ray parameter and travel time observations made in this study were useful in identifying the nature of the regional distance P coda waves, but were not of high enough quality to place meaningful constraints on Earth structure. A larger aperture array (i.e., YKA style of approximately 20 km) would improve the slowness resolution and perhaps lead to better results, however the existence of near-source scattered energy would still be problematic. In terms of constraining Earth structure from upper mantle triplications, a more fruitful approach is to use regional networks as wide-aperture arrays for a relatively small number of well-located, high-quality events. This gives record sections across large segments of distance with equivalent source signatures.

The most interesting work accomplished in this contract involved the

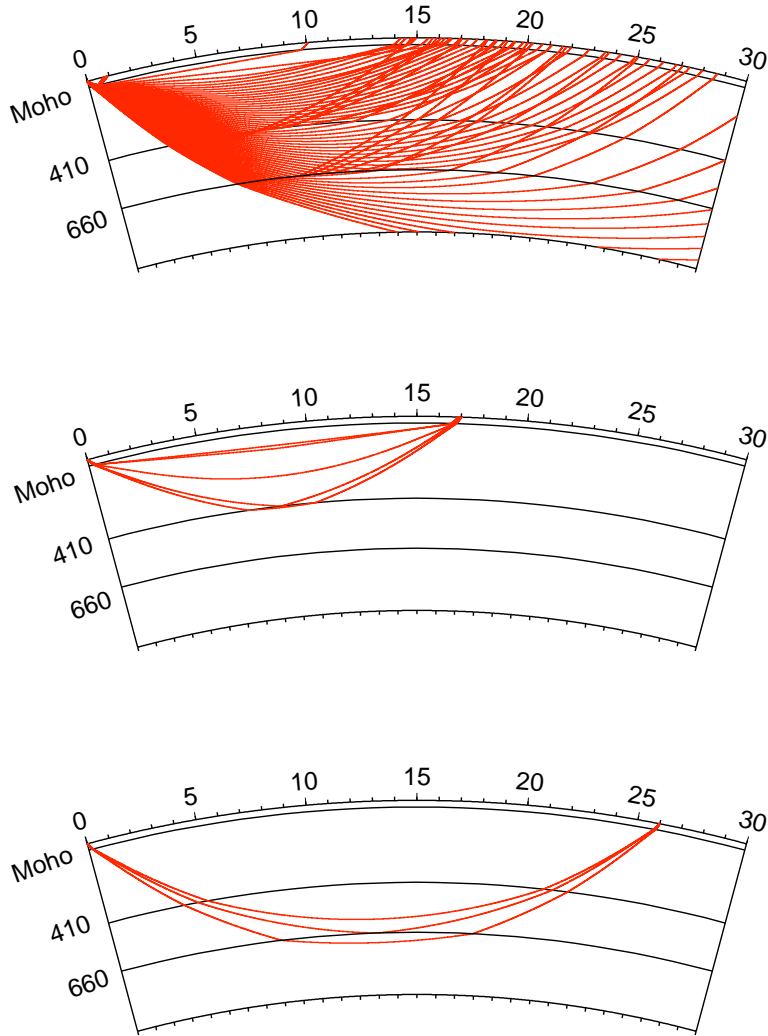
study of the ambient noise field at CMAR, in which we found strong anisotropy in both apparent velocity and backazimuth at frequencies smaller than about 1.4 Hz. Noise was peaked at velocities corresponding to teleseismic P waves and higher mode Rayleigh waves, while the ring of slowness space corresponding to regional distance P waves was relatively quiet. The Rayleigh noise arrived preferentially from the southwest and the east, while northern directions corresponding to the main Asian landmass were quiet. All the noise sources were well correlated with ocean wave heights, showing strong seasonal variation in power. Hence, detection thresholds at CMAR for teleseismic body waves and regional surface waves are seasonally and directionally dependent.

6 Acknowledgements

The work presented here was funded by the U.S. Air Force Research Laboratory under contract FA871806C0003. We thank the USNDC at AFTAC for making the CMAR data available. We are grateful to Dr. P.S. Callahan for assistance in working with the TOPEX/POSEIDON ocean wave height data. We used GMT (Wessel & Smith, 1991) to make most of the figures.

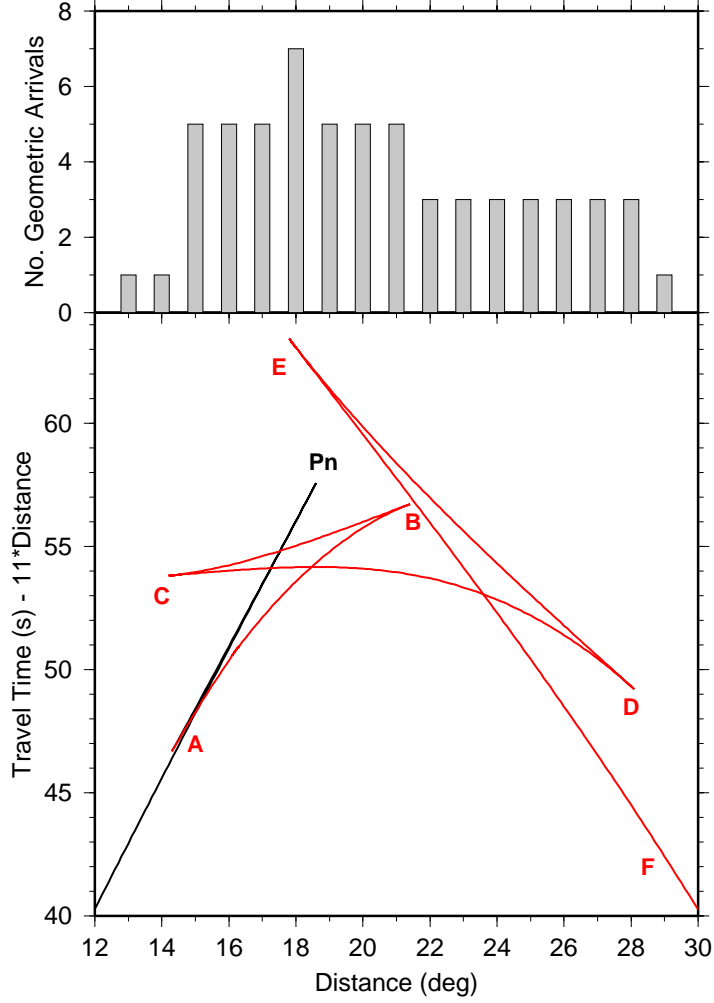
7 Figures

7.1 Transition Zone Ray Paths



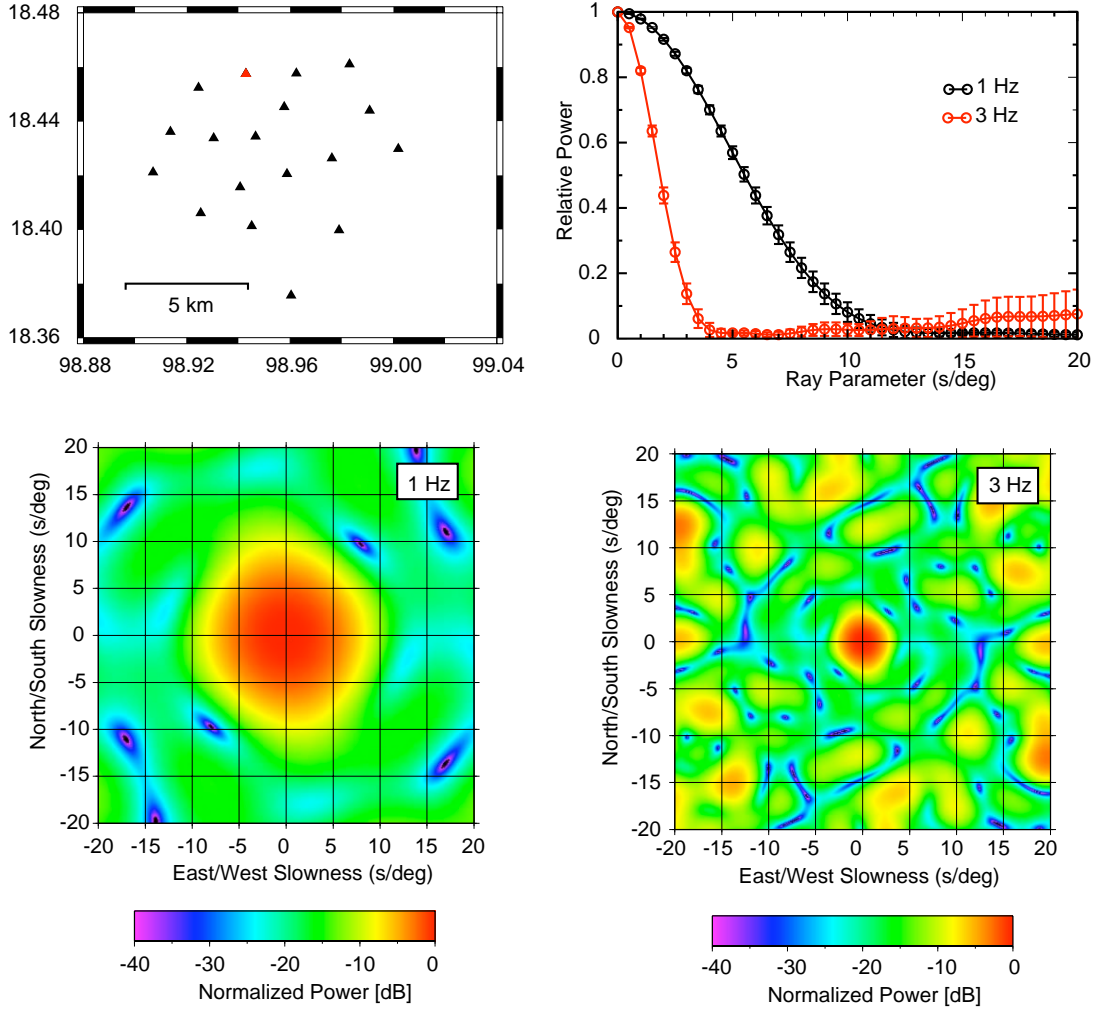
Ray paths through IASP91 for **(top)** ray parameters from 8.0-15.0 s/deg in increments of 0.05 s/deg, **(middle)** the five geometric rays predicted to exist at 17°, and **(bottom)** the three geometric arrivals predicted to exist at 26°.

7.2 Transition Zone Travel Time Curve



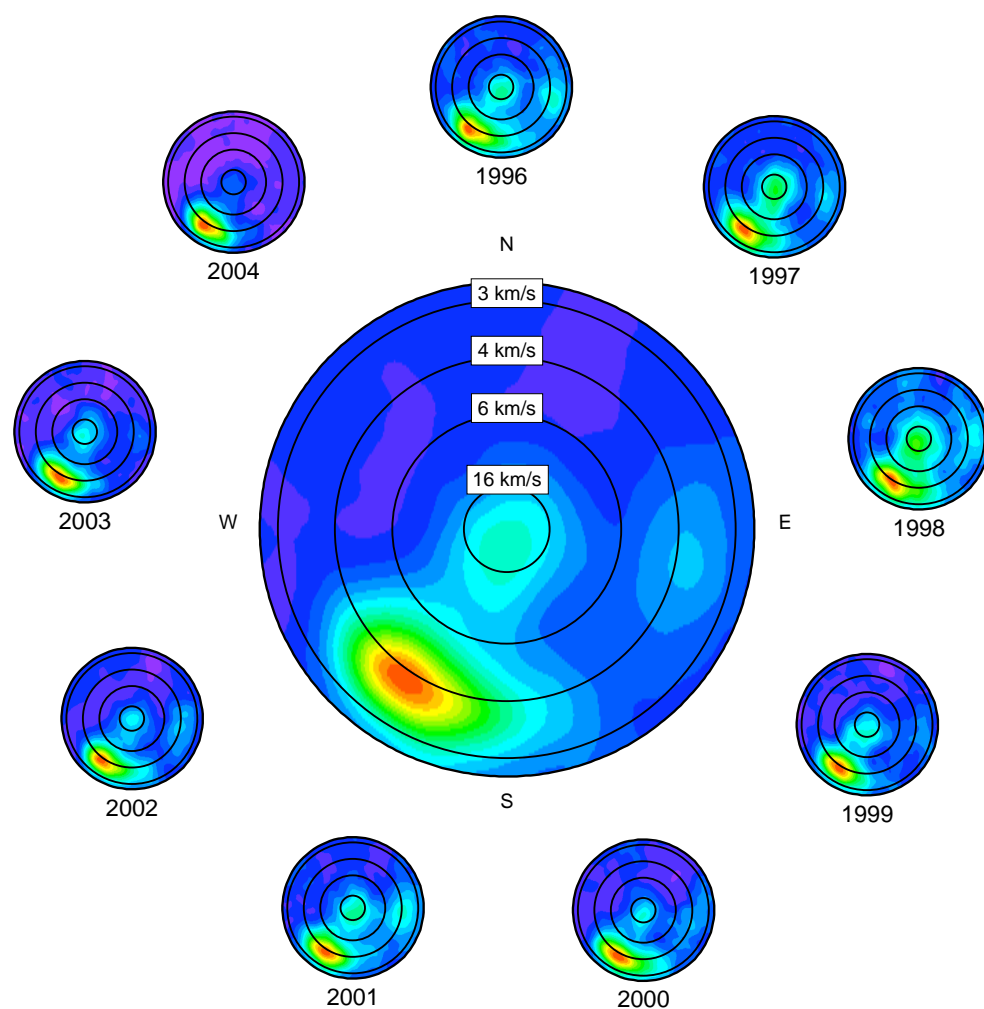
IASP91 travel time curve for a surface focus, reduced by 11 s/deg. Two asthenospheric branches merge at a cusp near 18.5° and we define this energy as P_n . In real data this sort of energy will be observable to larger distances and at slightly larger ray parameters as underside, whispering gallery reflections from the Moho contribute. The transition zone branches are shown in red and labeled A-F in order of decreasing ray parameter.

7.3 Array Response of CMAR



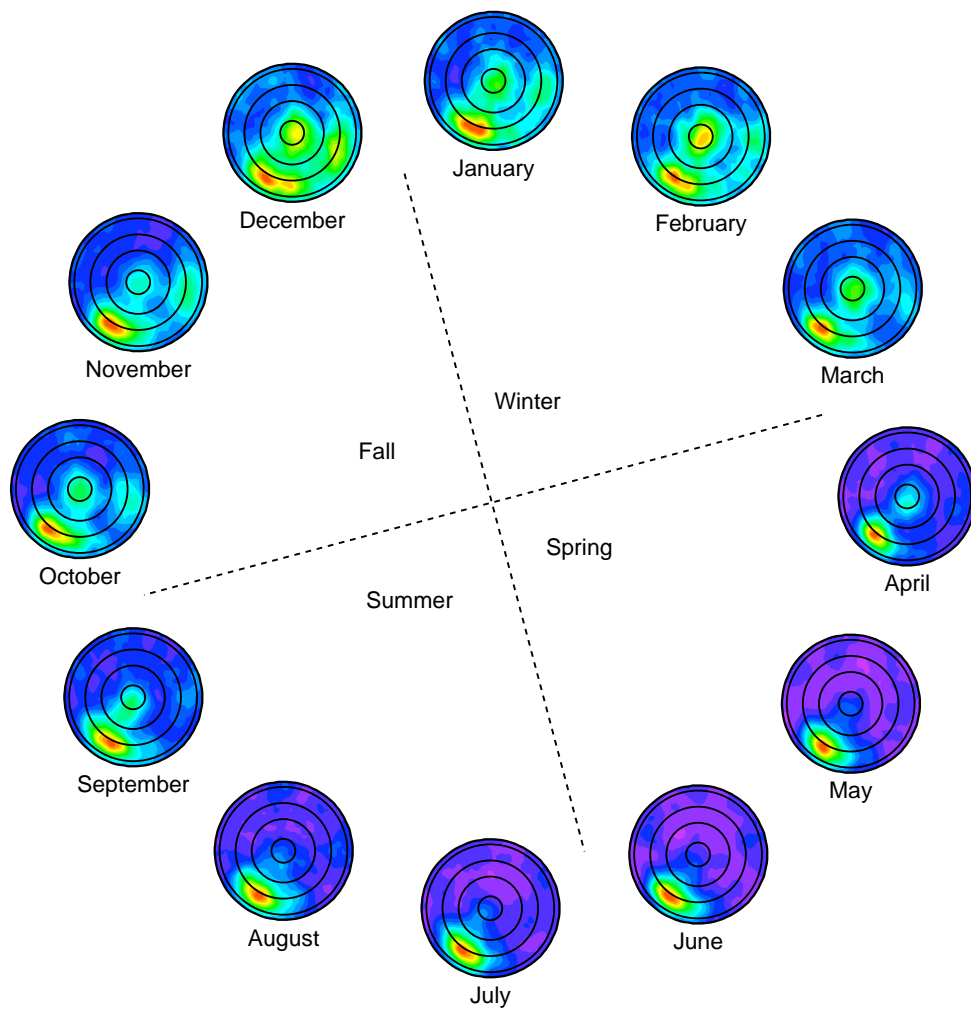
(upper left) Station geometry of CMAR and corresponding array response at (lower left) 1 Hz and (lower right) 3 Hz. (upper right) The azimuthally averaged array response at 1 Hz and 3 Hz.

7.4 Yearly Averages of Ambient Noise at CMAR



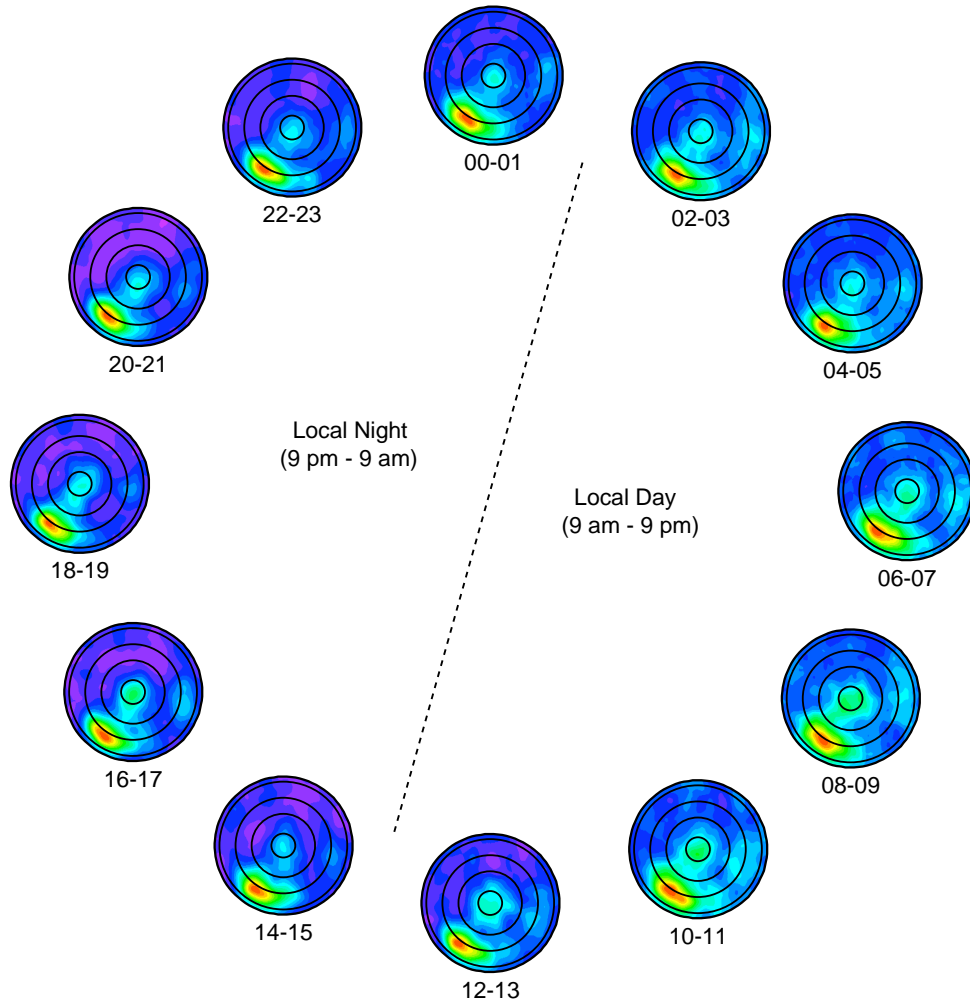
CMAR noise at 1 Hz averaged over nine years (**center**) and averaged in one-year bins. Amplitudes across slowness space are computed using phase-stack weighting and then normalized before being time-averaged.

7.5 Monthly Averages of Ambient Noise at CMAR



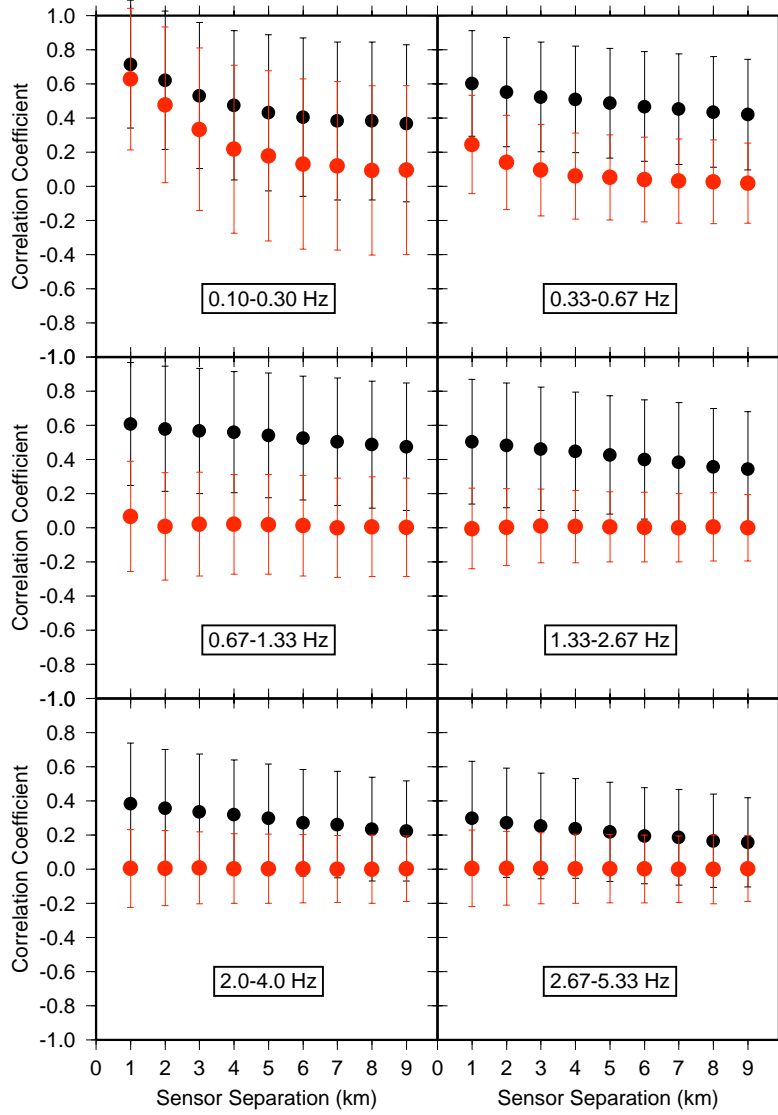
CMAR noise at 1 Hz from a nine-year period binned according to month. Amplitudes across slowness space are computed using phase-stack weighting and then normalized before being time-averaged.

7.6 Hourly Averages of Ambient Noise at CMAR



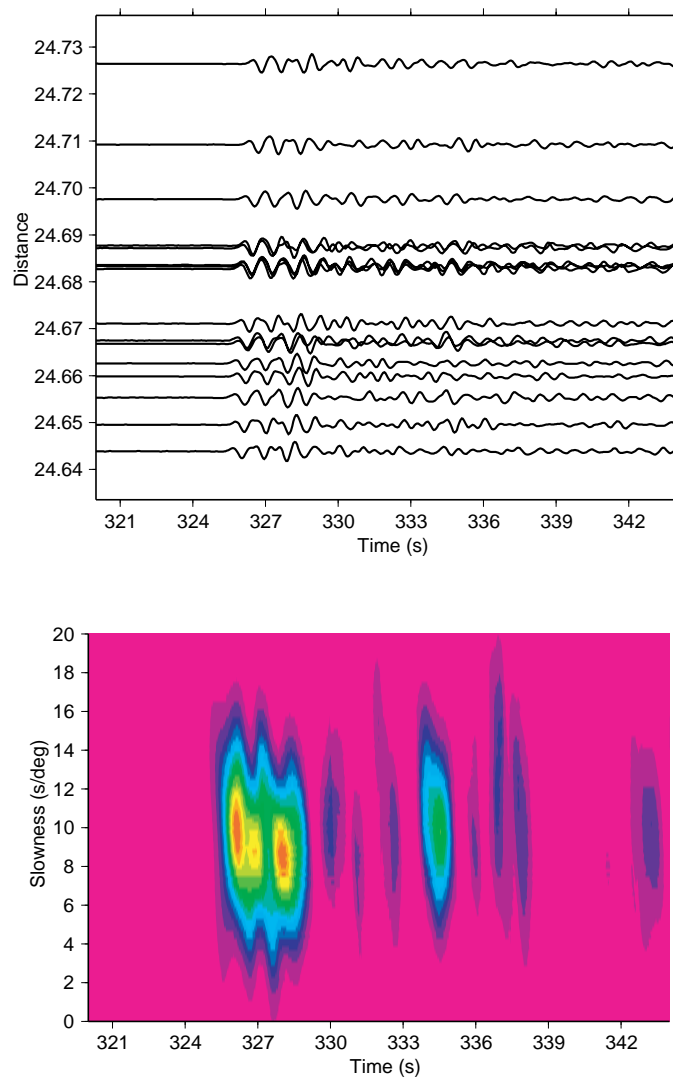
CMAR noise at 1 Hz from a nine-year period binned according to GMT hour. Amplitudes across slowness space are computed using phase-stack weighting and then normalized before being time-averaged.

7.7 Signal and Noise Coherence at CMAR



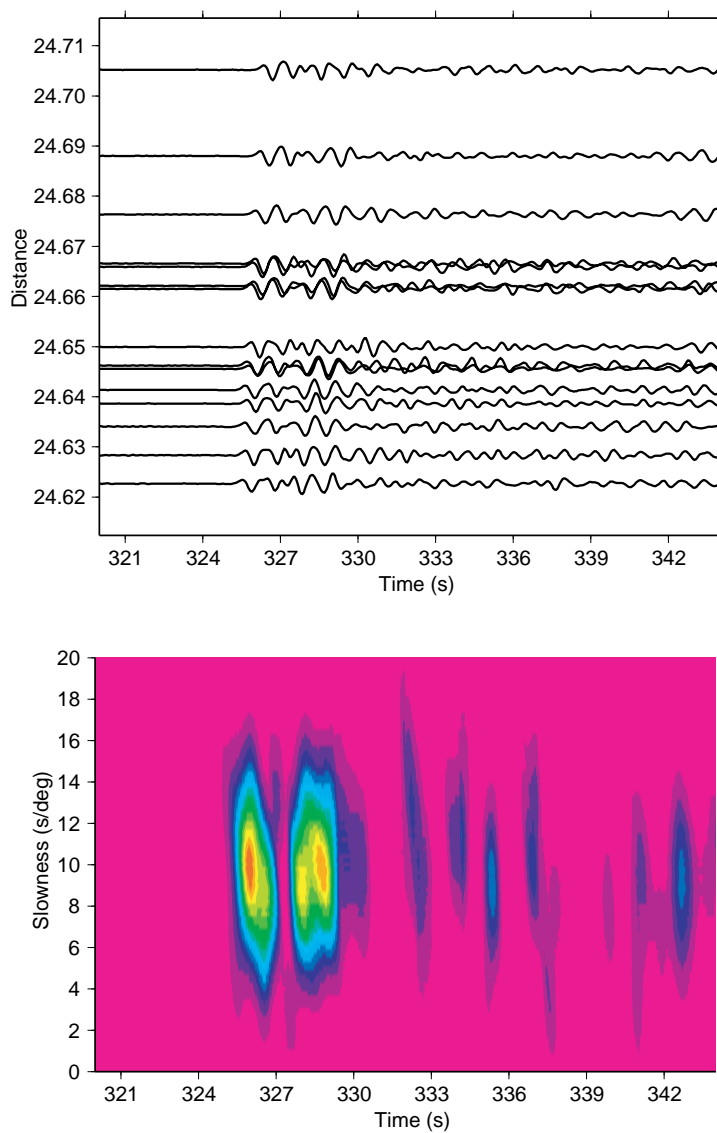
Correlation of signal (black) and noise (red) as a function of inter-element separation for six frequency bands. The signal was defined using a 10-s window around the first arrival for approximately 950 events to the northwest of CMAR, while the noise was defined using a 10-s window centered about a minute before the corresponding first arrival.

7.8 Chinese Nuclear Explosion of May 15, 1995



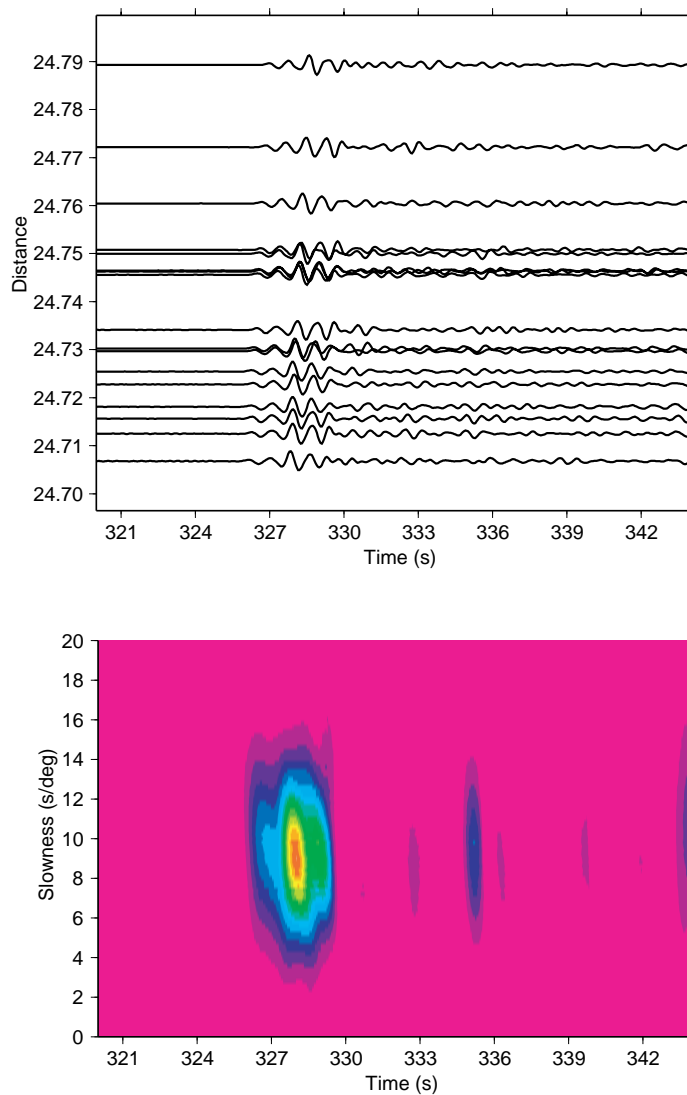
Record section and slantstack at CMAR for the Chinese nuclear explosion of May 15, 1995. The data were filtered with a 3-pole bandpass at 0.67-2.67 Hz and phase weighted stacking of order 3 was used.

7.9 Chinese Nuclear Explosion of August 17, 1995



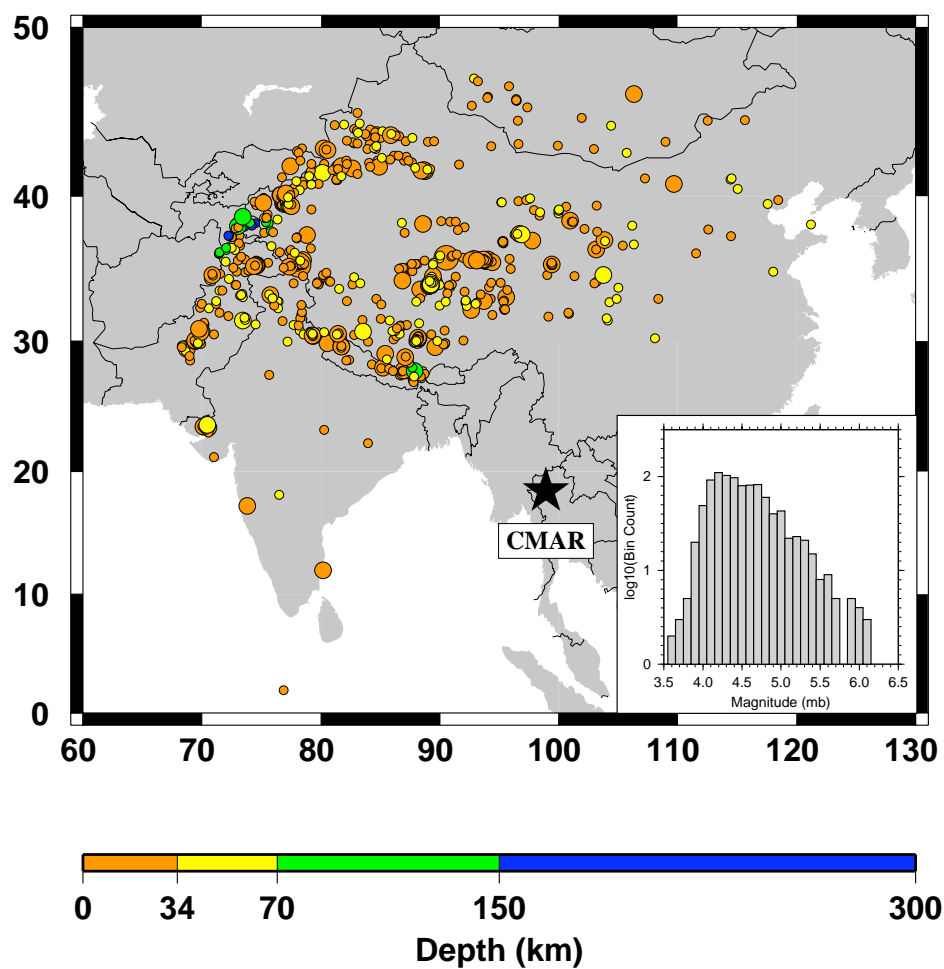
Record section and slantstack at CMAR for the Chinese nuclear explosion of August 17, 1995. The data were filtered with a 3-pole bandpass at 0.67-2.67 Hz and phase weighted stacking of order 3 was used.

7.10 Chinese Nuclear Explosion of June 8, 1996



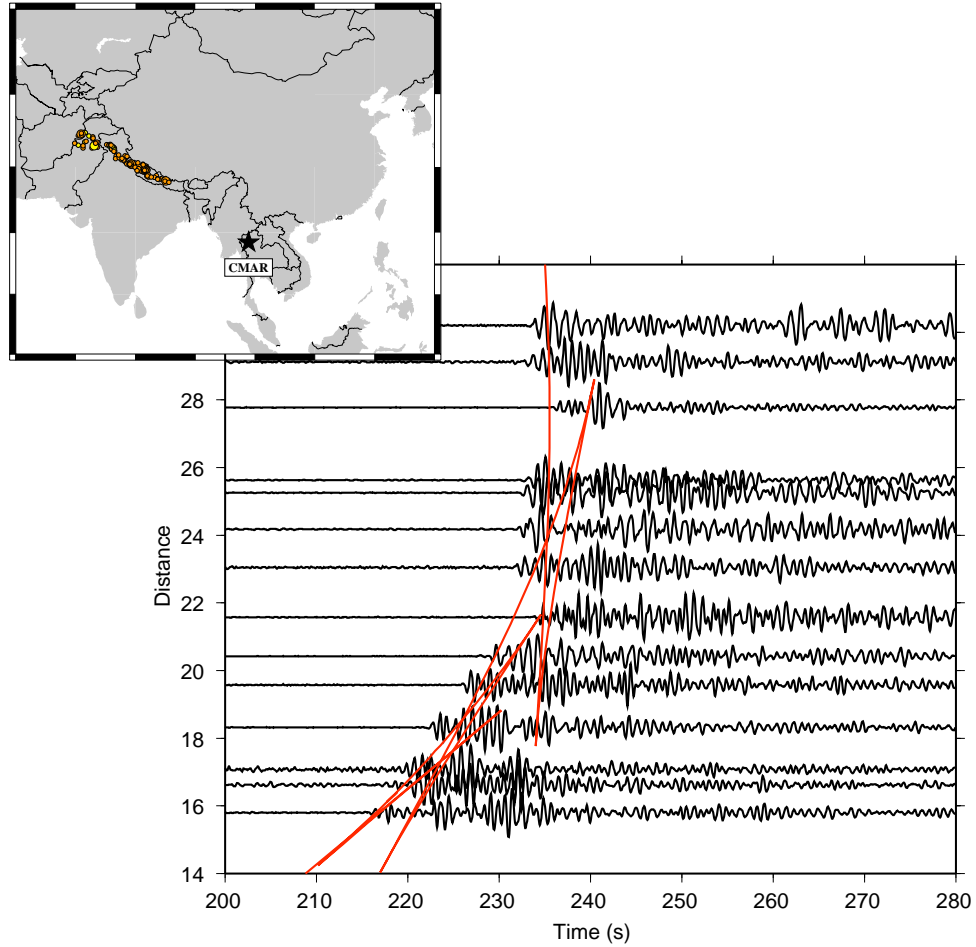
Record section and slantstack at CMAR for the Chinese nuclear explosion of June 8, 1996. The data were filtered with a 3-pole bandpass at 0.67-2.67 Hz and phase weighted stacking of order 3 was used.

7.11 Locations of EHB Events



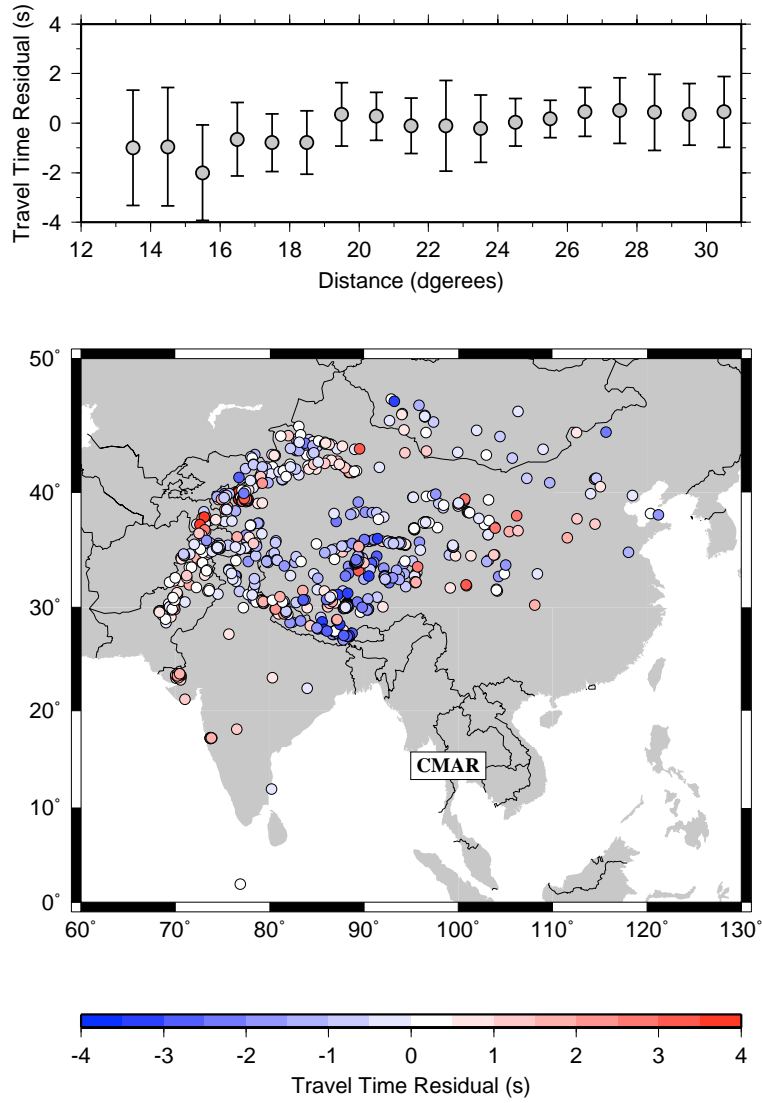
Locations of the 955 events from the EHB catalog that we considered in this study. Circle size is proportional to magnitude and, as shown in the inset, the catalog is complete down to a magnitude of about 4.7 mb.

7.12 Example Beam Record Section



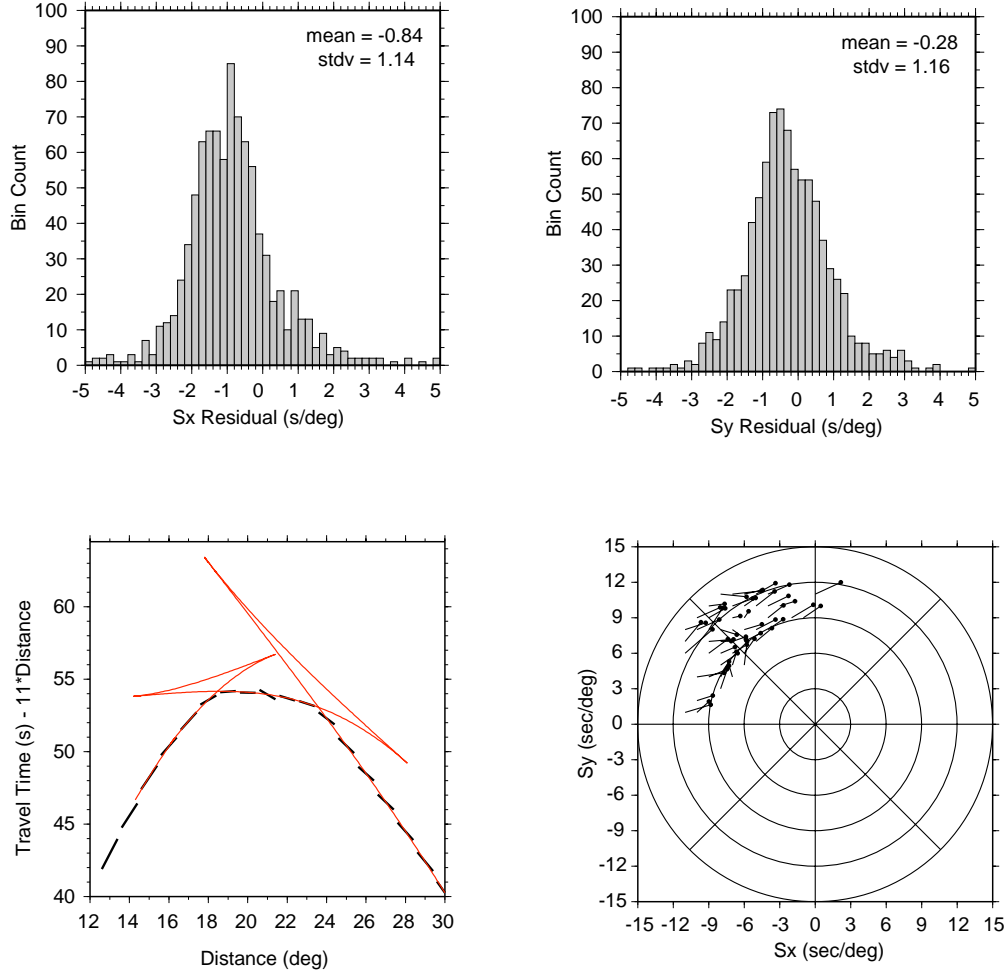
Example record section from a corridor of backazimuths at $305^\circ - 310^\circ$. The traces are phase-stack weighted beams formed at the expected slowness, and the red curve is the predicted travel time curve for IASP91. The times have been reduced by 8 s/deg.

7.13 Travel Time Residuals of First Arrivals



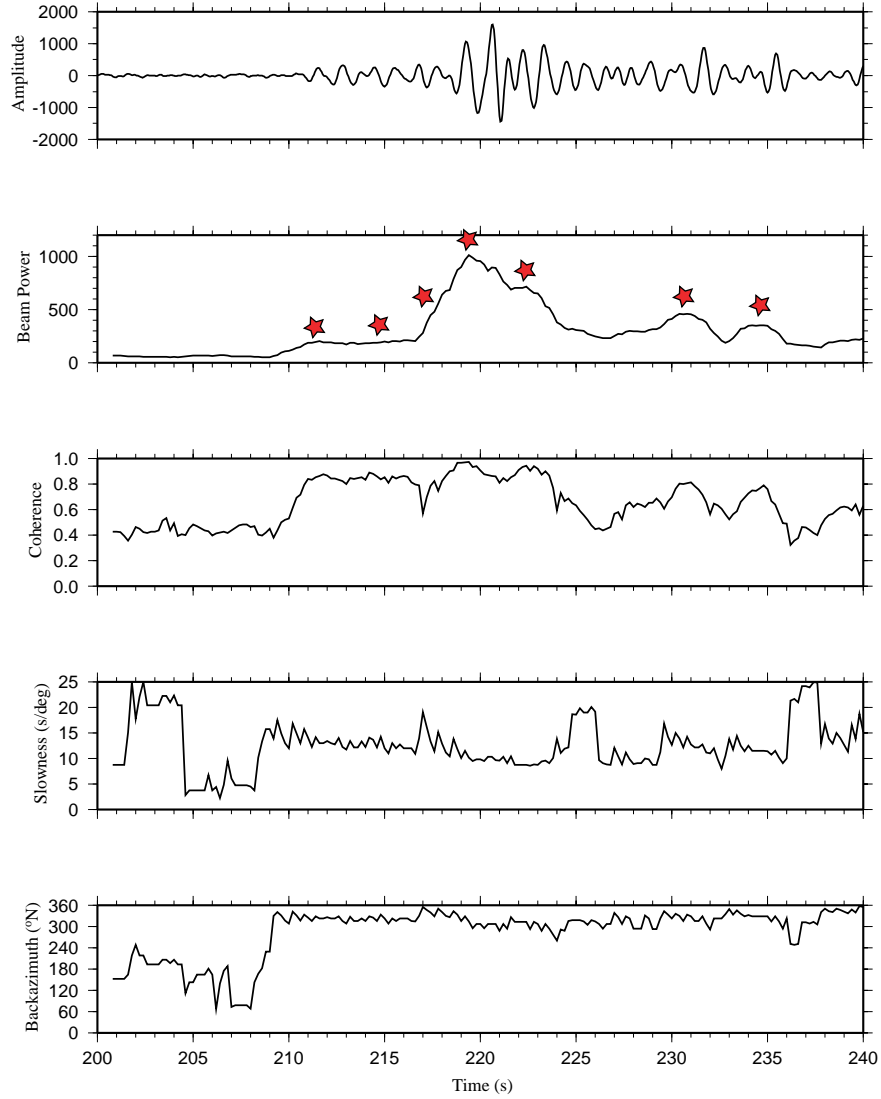
Travel time residuals, relative to IASP91, for the EHB data set considered in this study. The arrival times were handpicked and used to facilitate alignment of array beams.

7.14 Slowness Residuals of First Arrivals



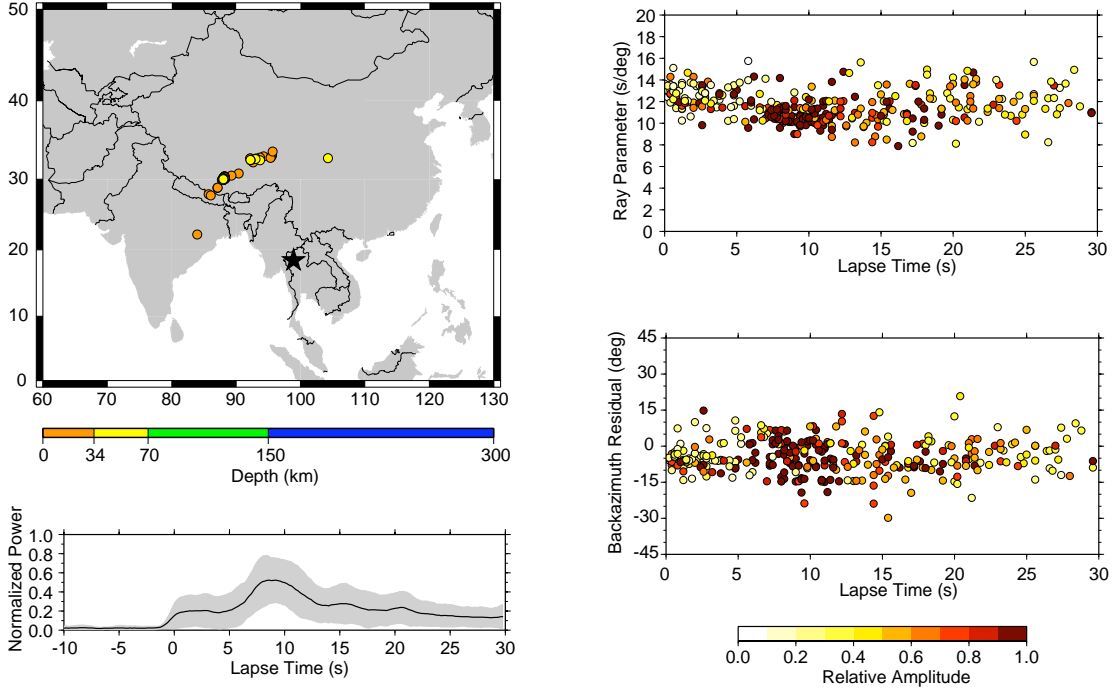
Slowness analysis of first arriving phases for the EHB data set. The two upper panels show histograms of slowness residuals in Cartesian coordinates, the lower left panel shows binned ray parameter estimates and predictions, and the lower right panel shown full vector slowness residuals in the manner of Bondar et al. (1999).

7.15 Example Sliding Window Slowness Analysis



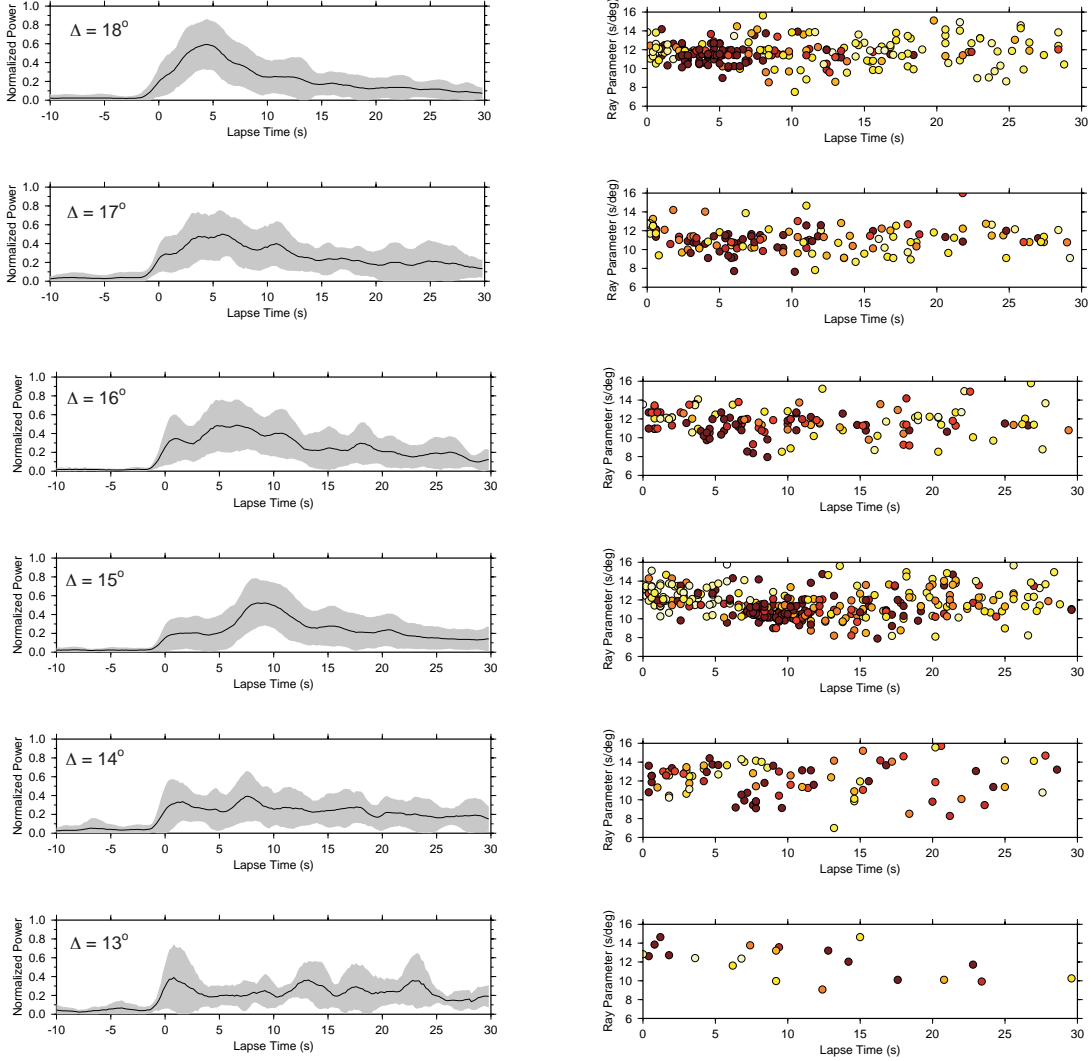
Example output from the sliding window slowness analysis of an event located 15.1° from CMAR. The top panel shows a simple linear beam formed at the expected slowness while the next four panels show beam power, coherence, ray parameters, and backazimuth as a function of time. The stars indicate arrivals picked by the automated algorithm described in the text.

7.16 Properties of P coda at Distances Near 15°



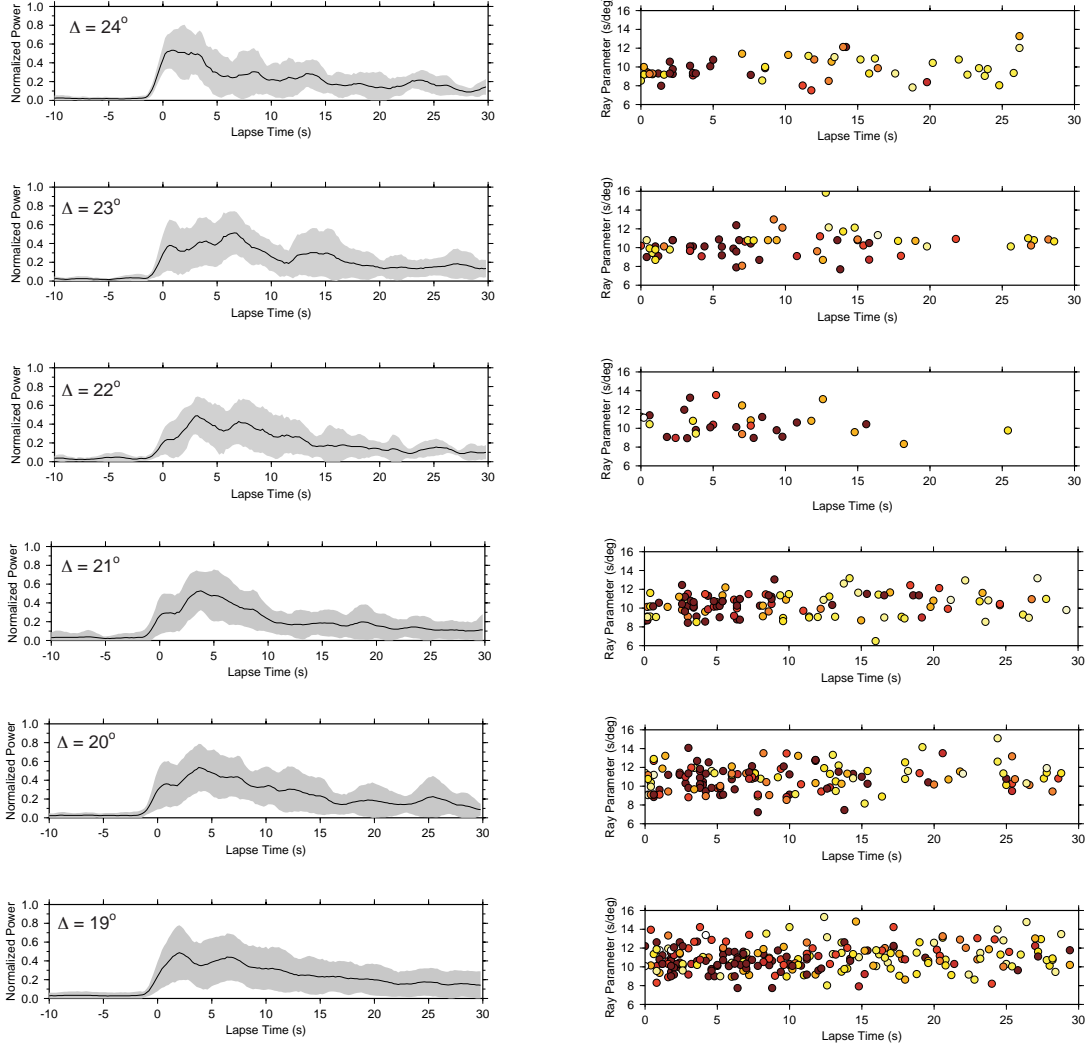
Coda properties for 83 shallow events that occurred at distances of $14.5^\circ - 15.5^\circ$ from CMAR. The upper left panel shows the event locations while the lower left panel shows a beam power stack. The grey area represents \pm one standard deviation. The panels on the right show the ray parameters and backazimuths for significant arrivals within the coda, as determined by the algorithm described in the text.

7.17 P coda at Distances of $13^\circ - 18^\circ$



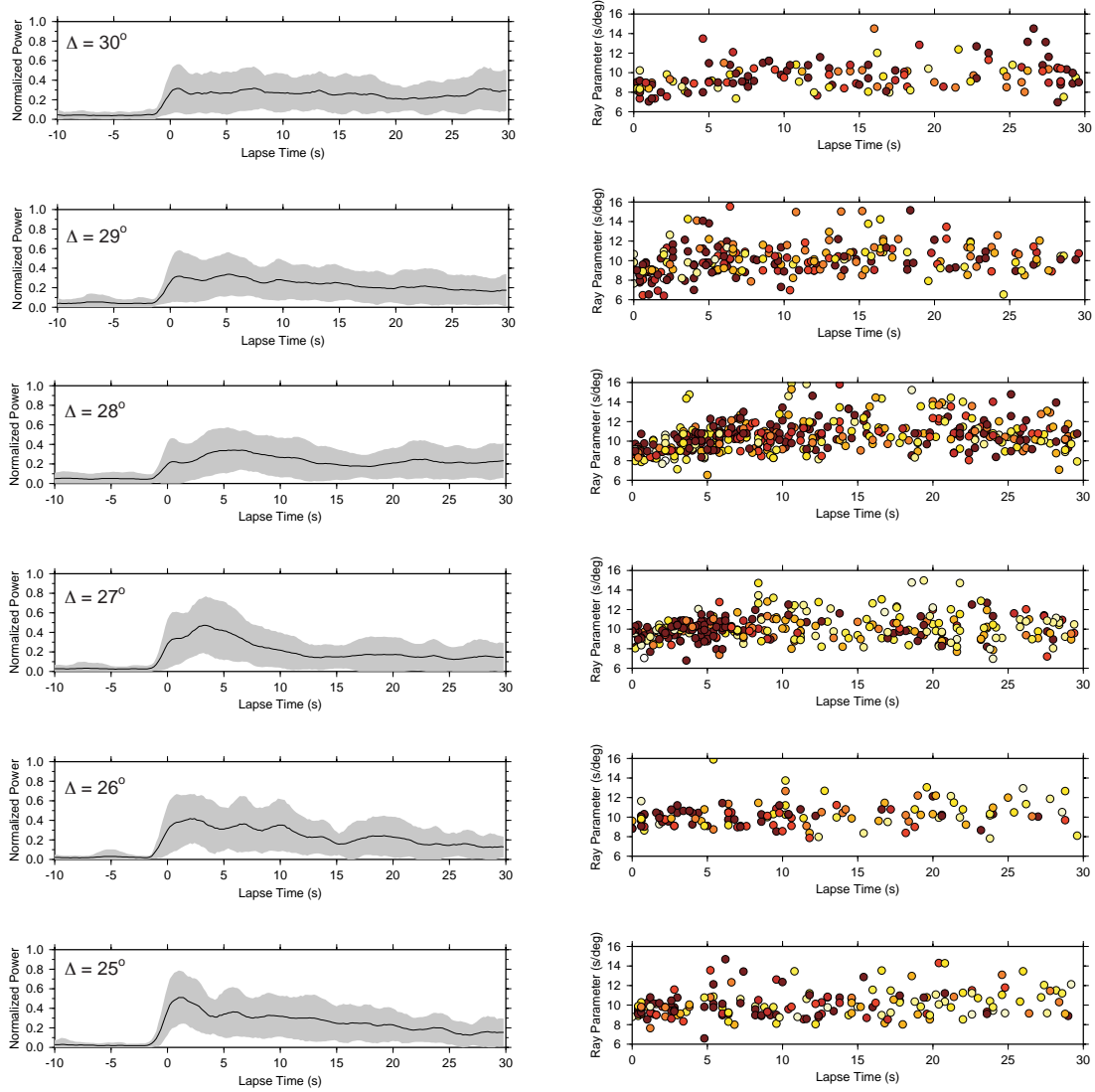
Panels on the left show stacks of beam power from events in various distance bins. The grey area indicates \pm one standard deviation. Panels on the right show the estimated slowness for significant arrivals in the coda.

7.18 P coda at Distances of $19^\circ - 24^\circ$



Panels on the left show stacks of beam power from events in various distance bins. The grey area indicates \pm one standard deviation. Panels on the right show the estimated slowness for significant arrivals in the coda.

7.19 P coda at Distances of $25^\circ - 30^\circ$



Panels on the left show stacks of beam power from events in various distance bins. The grey area indicates \pm one standard deviation. Panels on the right show the estimated slowness for significant arrivals in the coda.

References

- Bokelmann, G. H. R., 1995. Azimuth and slowness deviation from the GERES regional array, *Bull. Seismol. Soc. Am.*, **85**, 1456–1463.
- Bondar, I., North, R. G., & Beall, G., 1999. Teleseismic slowness-azimuth station corrections for the international monitoring system seismic network, *Bull. Seismol. Soc. Am.*, **89**, 989–1003.
- Bonner, J. L., Russell, D. R., Harkrider, D. G., Reiter, D. T., & Herrmann, R. B., 2006. Development of a time-domain, variable-period surface-wave magnitude measurement procedure for application at regional and teleseismic distances, part II: Application and Ms-mb performance, *Bull. Seismol. Soc. Am.*, **96**, 678–696.
- Buland, R. & Chapman, C. H., 1983. The computation of seismic travel times, *Bull. Seismol. Soc. Am.*, **73**, 1271–1302.
- Capon, J., 1969. High-resolution frequency-wavenumber spectrum analysis, *Proc. IEEE*, **57**, 1408–1418.
- Davies, D., Kelly, E. J., & Filson, J. R., 1971. Vespa process for analysis of seismic signals, *Nature Phys. Sci.*, **232**, 8–13.
- Deuss, A. & Woodhouse, J., 2001. Seismic observations of splitting of the mid-transition zone discontinuity in Earth’s mantle, *Science*, **294**, 354–357.
- Deuss, A. & Woodhouse, J. H., 2004. The nature of the Lehmann discontinuity from its seismological Clapeyron slopes, *Earth Planet. Sci. Lett.*, **225**, 295–304.
- Dziewonski, A. M. & Anderson, D. L., 1981. Preliminary reference earth model, *Phys. Earth Planet Int.*, **25**, 297–356.
- Engdahl, E., van der Hilst, R. D., & Buland, R. P., 1998. Global teleseismic earthquake relocation with improved travel times and procedures for depth determination, *Bull. Seismol. Soc. Am.*, **88**, 722–743.
- Filson, J., 1975. Array seismology, *Annu. Rev. Earth Planet. Sci.*, **3**, 157–181.

- Fisk, M., 2002. Accurate locations of nuclear explosions at the Lop Nor test site using alignment of seismograms and IKONOS satellite imagery, *Bull. Seismol. Soc. Am.*, **92**, 2911–2925.
- Gaherty, J. B. & Jordan, T. H., 1995. Lehmann discontinuity as the base of an anisotropic layer beneath continents, *Science*, **268**, 1468–1471.
- Ganguly, J. & Frost, D. J., 2006. Stability of anhydrous phase b: Experimental studies and implications for phase relations in subducting slab and the x discontinuity in the mantle, *J. Geophys. Res.*, **111**, B06203.
- Gupta, I. N., McElfresh, T. W., & Wagner, R. A., 1991. Near-source scattering of Rayleigh to P in teleseismic arrivals from Pahute Mesa (NTS) shots, in *Explosion Source Phenomenology, Geophysical Monograph 65*, edited by H. J. Patton & P. G. Richards, pp. 151–159, American Geophysical Union, Washington, D.C.
- Johnson, L. R., 1967. Array measurements of P velocities in the upper mantle, *J. Geophys. Res.*, **72**, 6309–6325.
- Karato, S., 1992. On the Lehmann discontinuity, *Geophys. Res. Lett.*, **19**, 2255–2258.
- Kennett, B. L. N. & Engdahl, E. R., 1991. Traveltimes for global earthquake location and phase identification, *Geophys. J. Int.*, **105**, 429–465.
- Koper, K. D. & de Foy, B., 2008. Seismic noise from Earth’s deep interior, *Bull. Seismol. Soc. Am.*, **submitted**.
- Lawrence, J. F. & Shearer, P. M., 2006. A global study of transition zone thickness using receiver functions, *J. Geophys. Res.*, **111**, B06307.
- Lefevre, L. V. & Helmberger, D. V., 1989. Upper mantle P velocity structure of the Canadian Shield, *J. Geophys. Res.*, **94**, 17749–17765.
- Mykkeltveit, S., Astebol, K., Doornbos, D. J., & Husebye, E. S., 1983. Seismic array configuration optimization, *Bull. Seismol. Soc. Am.*, **73**, 173–186.
- Niazi, M. & Anderson, D. L., 1965. Upper mantle structure of Western North America from apparent velocities of P waves, *J. Geophys. Res.*, **70**, 4633–4640.

- Ram, A. & Mereu, R. F., 1977. Lateral variations in upper-mantle structure around india as obtained from gauribidaur seismic array data, *Geophys. J. R. astr. Soc.*, **49**, 87–113.
- Ram, A., Mereu, R. F., & Wiechert, D. H., 1978. The identification and interpretation of upper-mantle travel-time branches from measurements of $dT/d\Delta$ made on data recorded at the yellowknife seismic array, *Can. J. Earth Sci.*, **15**, 227–236.
- Revenaugh, J. & Jordan, T. H., 1991. Mantle layering from ScS reverberations: 3. The upper mantle, *J. Geophys. Res.*, **96**, 19781–19810.
- Revenaugh, J. & Sipkin, S. A., 1994. Seismic evidence for silicate melt atop the 410-km mantle discontinuity, *Nature*, **369**, 474–476.
- Ringdal, F., 1981. Location of regional events using travel time differentials between P arrival branches, NORSAR Scientific Report No. 2, NTN/NORSAR, Kjeller, Norway.
- Rost, S. & Thomas, T., 2002. Array seismology; methods and applications, *Rev. Geophys.*, **40**, doi:10.1029/2000RG000100.
- Russell, D. R., 2006. Development of a time-domain, variable-period surface-wave magnitude measurement procedure for application at regional and teleseismic distances, part I: Theory, *Bull. Seismol. Soc. Am.*, **96**, 665–677.
- Ryberg, T., Wenzel, F., Egorkin, A. V., & Solodilov, L., 1997. Short-period observation of the 520 km discontinuity in northern Eurasia, *J. Geophys. Res.*, **102**, 5413–5422.
- Ryberg, T., Wenzel, F., Egorkin, A. V., & Solodilov, L., 1998. Properties of the mantle transition zone in northern Eurasia, *J. Geophys. Res.*, **103**, 811–822.
- Schimmel, M. & Paulssen, H., 1997. Noise reduction and detection of weak, coherent signals through phase-weighted stacks, *Geophys. J. Int.*, **130**, 497–505.
- Schmidt, R. O., 1986. Multiple emitter location and signal parameter estimation, *IEEE. Trans. on Antennas and Propagation*, **34**, 276–280.

- Schweitzer, J., Fyen, J., Mykkeltveit, S., & Kvaerna, T., 2002. Chapter 9: Seismic arrays, in *IASPEI New manual of seismological observatory practice*, edited by P. Bormann, p. 55, GeoForschungsZentrum Potsdam.
- Shearer, P. M., 1990. Seismic imaging of upper-mantle structure with new evidence for a 520-km discontinuity, *Nature*, **344**, 121–126.
- Shumway, R. H., Smart, E., & Clauter, D. A., 2008. Mixed signal processing for regional and teleseismic arrays, *Bull. Seismol. Soc. Am.*, **98**, 36–51.
- Simpson, D. W., Mereu, R. F., & King, D. W., 1974. An array study of P-wave velocities in the upper mantle transition zone beneath northeastern Australia, *Bull. Seismol. Soc. Am.*, **64**, 1757–1788.
- Song, T. A., Helmberger, D. V., & Grand, S. P., 2004. Low-velocity zone atop the 410-km seismic discontinuity in the northwestern United States, *Nature*, **427**, 530–533.
- Stead, R. J. & Helmberger, D. V., 1988. Numerical-analytical interfacing in two dimensions with application to modeling of seismicograms, *Pure Appl. Geophys.*, **128**, 157–193.
- Tichelaar, B. W. & Ruff, L. J., 1989. How good are our best models? Jackknifing, bootstrapping, and earthquake depth, *Eos Trans. AGU*, **70**, 605–606.
- van Decar, J. C. & Crosson, R., 1990. Determination of teleseismic relative phase arrival times using multi-channel cross-correlation and least squares, *Bull. Seismol. Soc. Am.*, **80**, 150–159.
- Walck, M. C., 1984. The P-wave upper mantle structure beneath an active spreading center: The Gulf of California, *Geophys. J. R. astr. Soc.*, **76**, 697–723.
- Wessel, P. & Smith, W., 1991. Free software helps map and display data, *Eos Trans. AGU*, **72**, 441, 445–446.
- Zhao, M., Langston, C. A., & Nyblade, A. A., 1999. Upper mantle velocity structure beneath southern africa from modeling regional seismic data, *J. Geophys. Res.*, **104**, 4783–4794.

9 Appendix

9.1 Preprint of Koper & de Foy (2008)

In this section we include a preprint of a manuscript that arose from this contract:

Koper, K.D., and B. de Foy, 2008. Seismic noise from Earth's deep interior, *BSSA*, under review.

It was submitted to *BSSA* on May 19, 2008 and is currently under review.

Seismic Noise from Earth's Deep Interior

Keith D. Koper^{*} and Benjamin de Foy

Dept. of Earth and Atmospheric Sciences, Saint Louis University,

3642 Lindell Blvd, St. Louis, MO 63108, USA

1 Abstract

2 We present an analysis of seismic noise recorded during 1995-2004 by a medium-
3 aperture, short-period seismic array located in Chiang Mai, Thailand (CMAR). We
4 calculated frequency-wavenumber spectra for nearly 1000 randomly selected time
5 windows, each with a length of 160 s. At frequencies above about 1.4 Hz the noise
6 is unorganized and wavenumber spectra are isotropic and diffuse; however, at lower
7 frequencies three robust wavenumber peaks exist. Two of the peaks have phase
8 velocities centered near 4.0 km/s, consistent with higher-mode Rayleigh waves,
9 while the third peak has much higher apparent velocity (>25 km/s), consistent
10 with waves that have interacted with Earth's core (PKP, PcP). All three peaks are
11 strongly seasonal with annual power variations of 10-20 dB, and all show excellent
12 correlation in their putative source regions with ocean wave heights derived from
13 TOPEX/POSEIDON satellite tracks. To the best of our knowledge, this is the first
14 time such a high-velocity component of seismic noise has been consistently observed.
15 The presence of this high-velocity peak raises the possibility of using ambient noise
16 to image Earth's lower mantle and core.

17 *Key words:* seismic noise, array seismology, south Asia, Earth's core, microseism

^{*} Corresponding Author: koper@eas.slu.edu; 314-977-3197

1 Introduction

Seismometer arrays have been used to study seismic noise at frequencies spanning more than three orders of magnitude, from as low as 0.002 Hz (Rhie & Romanowicz, 2004) to above 2 Hz (Okada, 2003). Arrays are exceptionally useful in noise studies because they provide directional constraints on propagating energy (Rost & Thomas, 2002). Measurements of apparent velocity allow body wave components of noise to be identified and distinguished from surface wave components (Toksoz & Lacos, 1968; Haubrich & McCamy, 1969; Lacos et al., 1969) and allow surface wave dispersion curves to be observed and inverted for geologic models of the subsurface (e.g. Louie, 2001). Measurements of backazimuth allow specific sources of seismic noise to be located (Bungum et al., 1971; Cessaro, 1994; Schulte-Pelkum et al., 2004) and even tracked as a function of time (Gerstoft et al., 2006).

Here we present an analysis of seismic noise recorded over a ten-year period at a seismic array in Chiang Mai, Thailand. Known as CMAR, the array is a primary station of the International Monitoring System (IMS) and is located at far-regional distances from nuclear test sites in China, India, Pakistan, and North Korea. Part of the motivation for this study is to determine noise characteristics at CMAR that might affect its nuclear monitoring capability. For instance, detection thresholds at CMAR likely depend significantly on the season, direction, and apparent velocity. More generally, the noise characteristics of CMAR are also interesting because they illuminate fundamental dynamic interactions among the oceans, atmosphere, and solid Earth (e.g. Webb, 1998).

42 2 Characteristics of CMAR

42 CMAR consists of 18 vertical-component seismometers arranged in a roughly
43 circular geometry (Figure 1a). The 153 inter-element separations range from
44 1.46 km to 10.07 km, and reflect a design goal of detecting teleseismic and
45 far-regional P waves at frequencies around 1 Hz. The corresponding array re-
46 sponse function (Figure 1b) is azimuthally symmetric and has sidelobes that
47 are small and well-separated from the main-lobe. Although CMAR is con-
48 sidered a medium-aperture array by the seismic monitoring community, the
49 inter-element separations are small enough that near receiver heterogeneities
50 can create travel time anomalies that are a significant fraction of the move-out
51 across the array. Potentially, this can lead to biased estimates of the slowness
52 vector. Examples of such heterogeneities observed at other arrays include a
53 dipping Moho (Tibuleac & Herrin, 1997), intra-array topography (Bokermann,
54 1995), and general variations in geology (Engdahl & Felix, 1971).

55 Fortunately, such slowness biases have been found to be relatively mild at
56 CMAR (Bondar et al., 1999). In that study, the authors compared observed
57 and predicted slowness vectors at CMAR for a large number of well-located
58 earthquakes and found a median ray parameter anomaly of -1.35 ± 0.58 s/deg
59 and a median backazimuth anomaly of $7.3 \pm 12.43^\circ$. Most of this bias can be
60 counteracted by applying corrections of -1.622 s/deg and 0.208 s/deg to ob-
61 servations of east-west and north-south slowness respectively. The bias can be
62 completely eliminated if additional, directionally dependent, corrections are
63 applied (Bondar et al., 1999). Therefore, energy peaks in frequency-wavenumber
64 spectra observed at CMAR can be confidently backprojected to general geo-
65 graphical regions.

3 Computing Frequency-Wavenumber Spectra at CMAR

We extracted 955 time windows of seismic noise recorded at CMAR from 1995 through 2004. The 160-s long windows were chosen to end several tens of seconds in advance of P waves from a population of regional distance earthquakes that were analyzed in a related study. The time windows occur in all months, years, and hours of the day, and have a quasi-random distribution. All the data were visually inspected and channels that had glitches or null segments were removed. An average of 15.2 channels per noise window were acceptable.

We used two complementary methods to study the slowness of the CMAR seismic noise. The first is a classic frequency domain method (Capon, 1969) that averages over time and has relatively high resolution in frequency. The second is a time domain beampacking method (e.g., Schweitzer et al., 2002) that averages over frequency and has relatively high resolution in time. For both methods we assumed that the seismic noise was stationary in time and space over the sample interval. We also ignored elevation differences among the array elements and considered only 2D wavenumber vectors. This is appropriate because CMAR is relatively flat, having a maximum elevation difference of only 0.066 km, compared to a horizontal aperture of 10.1 km (see Bokelmann (1995) for a discussion of topographic effects on slowness inference).

The frequency domain technique is a high-resolution, direct segment approach (Capon, 1969) described as follows. For each of the 18 channels of CMAR data we extract 3200 data points and subdivide them into 25 non-overlapping, adjacent subwindows of 128 samples each. The sampling interval at CMAR is 0.05 s, so each subwindow is 6.4 s long and the total window length is 160 s. For

90 each subwindow and channel the mean is removed, a Bartlett taper is applied,
 91 and a Fast Fourier Transform (FFT) is calculated. For each subwindow, the
 92 18-by-18 spectral matrix is calculated by multiplying the FFT of each channel
 93 by the complex conjugate of the FFT of every other channel. These 25 spectral
 94 matrix estimates are then linearly averaged to produce a single estimate with
 95 reduced variance. Also, by averaging more subwindows (25) than channels (18)
 96 the spectral matrix estimate will normally become nonsingular. Finally, the
 97 matrix is normalized by dividing each element, S_{jl} , by $\sqrt{S_{jj}S_{ll}}$. This corrects
 98 for unequal gain among the seismometers at CMAR.

99 For a given wavenumber vector, $\mathbf{k} = (k_x, k_y)$, and frequency, f_p , the power
 100 spectrum is defined as,

$$101 \quad P(f_p, \mathbf{k}) = \frac{1}{J^2} \sum_{j=1}^J \sum_{l=1}^J w_l(f_p) w_j^*(f_p) S_{jl}(f_p) e^{2\pi i \mathbf{k} \cdot (\mathbf{x}_j - \mathbf{x}_l)} \quad (1)$$

102 where \mathbf{x}_j is the position vector of the j^{th} seismometer relative to the array
 103 reference point, and J is the number of channels (18). This expression can
 104 also be written as a single sum if the set of all spatial difference vectors,
 105 called the coarray, is defined. The element weights, w_j , define a 2D spatial
 106 windowing function that is analogous to the Bartlett taper applied in the time-
 107 domain before the FFT. Here we use expressions developed for a maximum
 108 likelihood filter that passes energy at a given wavenumber in an optimal least-
 109 squares sense (Capon, 1969). Discussions of various strategies for choosing
 110 these weights are given elsewhere (Burg, 1964; Haubrich, 1968; Ingate et al.,
 111 1985; Douglas, 1998).

112 With the time windows chosen in this work, the frequency interval at which

123 $P(f_p, \mathbf{k})$ is calculated is 0.16 Hz. For a given frequency, we define a wavenum-
 124 ber grid such that the corresponding slowness grid varies from -40 s/deg to
 125 40 s/deg in increments of 0.5 s/deg, and evaluate $P(f_p, \mathbf{k})$ and at each node.
 126 The grid is set up in Cartesian coordinates and aligned such that the x compo-
 127 nent of slowness ($s_x \equiv k_x/f_p$) is East/West, and the y component of slowness
 128 ($s_y \equiv k_y/f_p$) is North/South. The backazimuth is defined clockwise from North
 129 as $\text{atan}(s_x/s_y)$, and the ray parameter is defined in units of s/deg as $\sqrt{s_x^2 + s_y^2}$.
 130 We also define the apparent or phase velocity in units of km/s as the inverse
 131 of the ray parameter.

132 The time domain technique is based on algorithms previously developed for
 133 analysis of coda waves and small amplitude body waves (Koper et al., 2004).
 134 In this approach we first extract time windows of length 64 s from each of
 135 the 18 channels at CMAR. For each trace we remove the mean, apply a 3
 136 pole Butterworth bandpass filter, and resample the data from 0.05 s to 0.01 s.
 137 The corner frequencies of the filter are either 0.33-0.67 Hz, 0.67-1.33 Hz, or
 138 1.33-2.67 Hz. A slowness grid with the same dimensions as used previously is
 139 constructed and a phase stack weighted beam (Schimmel & Paulssen, 1997) of
 140 order three is formed at each node. The power is defined as the mean-square
 141 amplitude of the beam over the 64 s time window. This approach is more
 142 computationally intensive than the frequency domain approach, which is why
 143 we use a shorter time window (64 s vs. 160 s). In all cases, the window for
 144 the time domain method is chosen as the first 64 s of the corresponding 160 s
 145 window.

146
 147 Example spectra are shown in Figure 2 for a typical time window. Power is
 148 plotted in decibels relative to the sample maximum, $10 \times \log_{10}(P/P_{\text{max}})$, and

the color scale is chosen such that only energy at least 10% of the maximum is highlighted. Agreement between the techniques is good, especially considering that the time and frequency sensitivities are different. The time-domain technique gives slightly sharper images, probably because it amplifies coherent energy via phase-weighted stacking. In both methods, at higher frequencies the noise power becomes diffuse and unorganized while at lower frequencies there are specific preferred directions. As we discuss later, the preferred noise directions at CMAR are generally stable from one time window to the next, though the absolute amplitudes exhibit strong variability.

4 Ocean Wave Heights From TOPEX/POSEIDON Data

To help interpret noise peaks observed in fk-spectra at CMAR we used a global model of ocean wave height determined from satellite data. Since ocean waves play a dominant role in generating microseismic noise, it follows that wave heights in oceanic source regions should have high correlation with time series of the corresponding microseismic energy. On the other hand, oceanic regions with wave heights that show poor or negative correlations with microseismic energy can be eliminated as potential source regions.

Significant Wave Heights, defined as the mean height of the highest 33% of ocean waves, were obtained from the Ku-band of the TOPEX/POSEIDON satellite altimetry mission (Callahan et al., 1994) via the merged geophysical data record (MGDR), distributed by the NASA Jet Propulsion Laboratory (JPL). The satellite has a 10-day repeat orbit with a maximum orbiting latitude of 66° , and data reported every second are averages of the values obtained from 10 Hz measurements. Using data for which at least 6 values were used

163 in the average, and for which the root mean square error of the 6 or more
 164 values was below 1 m, we calculated average monthly ocean wave heights over
 165 a 2° by 2° grid for the same ten year period (1995-2004) as the seismic noise
 166 data. Excluding grids that contained some fraction of land cover, and those
 167 that were beyond $\pm 60^\circ$ in latitude and so less robust, this led to 8,488 distinct
 168 time series of ocean wave height.

169 5 Interpretation of FK-spectra at CMAR

170 5.1 Average Results

171 Noise power as a function of slowness is shown in Figure 3 as an average
 172 over the 955 time windows. Individual spectra were normalized before con-
 173 tributing to the stack, therefore the relatively few windows that inadvertently
 174 contain large, earthquake generated signals do not bias the overall result. At
 175 frequencies above about 1.4 Hz the noise is incoherent and isotropic, and the
 176 two methods give dissimilar results. However, at lower frequencies the seis-
 177 mic noise is strongly anisotropic, relative to both backazimuth and apparent
 178 velocity, implying that it is organized as propagating plane waves.

179 At lower frequencies the two methods give similar results, showing three dis-
 180 tinct, robust peaks. These peaks are broadened somewhat, because each noise
 181 source varies within a general geographic region, however each of the three
 182 noise sources is clearly localized as shown by the sharpness of the correspond-
 183 ing histograms of peak noise power (Figure 4). In that figure we also show the
 184 effect of the slowness corrections of Bondar et al. (1999). We implemented the
 185 default correction to all observations and further applied the directionally de-

pendent corrections to those observations falling within the appropriate bins in slowness space. As expected, the corrections have little effect on the overall pattern of noise peaks.

It is important to emphasize that none of the three noise peaks shown in Figures 3 and 4 are sidelobes of one another. This is evident by examining the CMAR array transfer function, shown in Figure 1b at 1 Hz, and realizing that at lower frequencies the sidelobes are even more distant in slowness space. Furthermore, both of the spectral estimation techniques we used reduce the amplitude of spurious peaks, with the frequency domain technique in particular essentially deconvolving the array transfer function from the observed spectra (Capon, 1969).

5.2 *Rayleigh Noise from the East*

The weakest of the three noise peaks shown in Figure 3 has apparent velocities centered near 4.0 km/s (indicative of higher mode Rayleigh waves) and arrives from the east at backazimuths of $80^\circ - 120^\circ$. The seismically estimated source area for this Rayleigh energy is shown in Figure 5 as a wedge-shaped region extending eastward from CMAR across Vietnam into the South China Sea. We arbitrarily bounded the source region at a distance of 20° because of the high attenuation of short-period Rayleigh waves.

Surface waves are commonly observed in microseismic noise and excitation of the double frequency mode, centered at periods of 6-10 s, can be explained by counter-propagating ocean waves that interfere in a nonlinear manner (Longuet-Higgins, 1950). Our observations fall on the short-period side of

209 this peak, but can nevertheless be explained, for instance, by the interference
 210 of ocean waves incident on and reflected by the Vietnamese coastline. Little
 211 seismic noise is observed from the northern Vietnamese coast in the Gulf of
 212 Tonkin, which is presumably shielded from the Pacific Ocean by the island of
 213 Hainan. Likewise, the main island of Malaysia probably acts as a buffer to the
 214 south.

215 The time dependence of the seismic noise power is shown by the black curve
 216 in the bottom of Figure 5. For each time window we calculated the maximum
 217 noise power in the relevant region of slowness space and then normalized each
 218 estimate by the median of the population. We removed nearly 20 samples that
 219 were more than 20 dBs above the median, to eliminate the effect of earthquake
 220 energy, and averaged the remaining samples into monthly bins. The signal is
 221 strongly seasonal with peaks in local winter and troughs in local summer, and
 222 has a dynamic range of 10-15 dB. As shown in Figure 5, the seasonality of
 223 the seismic noise power is well matched by seasonal variations in ocean wave
 224 height in the South China Sea. The sample correlation coefficient between the
 225 two time series is 0.58, which is above the 99.9% level of significance using a
 226 Student-t test.

227 *5.3 Rayleigh Noise from the Southwest*

228 The largest noise peak shown in Figures 3 arrives from the southwest at back-
 229 azimuths of $180^\circ - 225^\circ$ and also has phase velocities centered near 4.0 km/s.
 230 The inferred source region is indicated by the wedge shape in Figure 6. Ge-
 231 ographically it corresponds to the Burmese coastline from the border with
 232 Thailand in the south to the peninsular Pagoda Point in the north. At slightly

233 larger backazimuths of $230^\circ - 280^\circ$ relatively little seismic noise is generated
 234 even though the nearby coastlines of western Burma, Bangladesh, and north-
 235 eastern India lie in this direction. Likewise, there is relatively little seismic
 236 noise generated at backazimuths of $135^\circ - 180^\circ$, corresponding to coastlines
 237 of the Malay Peninsula and the Gulf of Thailand. These two seismically quiet
 238 regions are likely shielded from northeasterly travelling storms by Sri Lanka
 239 and Indonesia respectively, while the narrow region in between is subjected
 240 directly to the prevailing currents and swell of the larger Indian Ocean.

241 The time dependence of the Indian Ocean seismic noise was calculated in the
 242 same manner as for the Pacific Ocean noise and is shown at the bottom of
 243 Figure 6. The median of these values is 4.1 times larger than the median of
 244 the Pacific Ocean values. Two factors are likely responsible for the increased
 245 power. First, there is larger fetch across the Indian Ocean than the South
 246 China Sea so the excitation of the Rayleigh energy on the southern Burmese
 247 coast is probably stronger than the excitation along the Vietnam coast. Sec-
 248 ond, the seismic propagation path from coastline to CMAR is shorter for
 249 the Indian Ocean noise source, and so lower attenuation of the short-period
 250 Rayleigh energy is expected.

251 Like the Pacific Ocean noise, the Indian Ocean noise is strongly seasonal with
 252 a dynamic range of 10-15 dB; however, the seasonal variation is opposite,
 253 with peaks in local summer and troughs in local winter. This phenomenon
 254 is well explained, though, by the seasonal variation of wave heights in the
 255 Indian Ocean, which peak in the northern summer (southern winter) because
 256 the Indian Ocean as a whole has southern hemisphere dynamics. Thus the
 257 seasonal anticorrelation of wave heights in the Pacific and Indian Oceans is
 258 mimicked by the seasonal anticorrelation of seismic noise from these regions.

260 The third noise peak shown in Figure 3 occurs near the center of the diagram,
261 indicating energy that is almost vertically incident on the array. Ray param-
262 eters for this peak are clustered between 0 and 5 s/deg, with a mean near
263 2.5 s/deg for the uncorrected data (Figure 4c) and a mean near 3.5 s/deg for
264 the corrected data (Figure 4d). Owing to the near-vertical incidence the back-
265 azimuths are poorly resolved, though there is a trend towards the southeast.
266 The ray parameter for P waves that turn just above the core-mantle bound-
267 ary (equivalently P_{diff}) is about 4.4 s/deg, so the fact that we observe smaller
268 values implies that the noise is composed of P waves that have interacted with
269 Earth’s core.

270 We first consider the possibility that the waves have been transmitted through
271 the core as PKP waves, and assume that the noise source occurs at a distance
272 of $140^\circ - 145^\circ$ from CMAR, as shown in Figure 7. This range brackets the
273 $PKP - B$ caustic, a distance at which energy is geometrically focused to a
274 maximum by the velocity structure in Earth’s core. We note that previous
275 observations of P waves in microseismic noise have generally occurred at ray
276 parameters consistent with a distance of 20° (Haubrich & McCamy, 1969;
277 Gerstoft et al., 2006), a range in which body wave energy is also geometrically
278 focused, in this case by high velocity gradients in the mantle transition zone.

279 The time dependence of the P-wave noise is shown by the black line in the
280 bottom of Figure 7. It was calculated, in the manner described earlier, from the
281 region of slowness space with velocity greater than 20 km/s (ray parameter
282 less than 5.5 s/deg), and it has a median that is 3.1 times larger than the

283 median of the Pacific Ocean Rayleigh noise. There is a clear seasonality to
 284 the seismic noise, with peaks in the northern winter and troughs in northern
 285 summer, though the dynamic range is only 5-10 dB. The correlation of the
 286 seismic noise with ocean wave heights across the hypothetical PKP source
 287 region is also shown in Figure 7. While it is tempting to suggest that the
 288 strong waves near the southern tip of South America create PKP noise at
 289 CMAR, no significant correlation was found with the seismic observations.
 290 The only portion of the seismic source annulus that gives high correlation
 291 is the patch along the northern coast of Brazil near the Amazon delta. The
 292 sample correlation coefficient for this area is 0.44, which is significant above
 293 the 99.9% level.

294 A potential problem with this interpretation though is that it corresponds to
 295 northwesterly backazimuths at CMAR. The data prefer southeasterly backaz-
 296 imuths (Figure 4), corresponding to the southwestern quadrant of the seismic
 297 source annulus shown in Figure 7. Therefore, for this interpretation to be cor-
 298 rect it must be the case that our slowness estimates are biased (on the order
 299 of 3-4 s/deg) by imperfections in the slowness corrections of Bondar et al.
 300 (1999), or because of some deficiency in our observational techniques. For ex-
 301 ample, our slowness inference techniques assume a single plane wave model
 302 and if multiple plane waves arrive in the same time window it is possible that
 303 the peak of the dominant arrival is shifted somewhat in slowness space (e.g.,
 304 Shumway et al., 2008).

305 We next consider the possibility that the high-velocity noise peak observed at
 306 CMAR is created by energy that has reflected off the core-mantle boundary as
 307 PcP waves. This seems less plausible than the PKP hypothesis because PcP
 308 waves are relatively small, especially at small source-receiver distances, and

the corresponding direct P waves would be expected to be visible in the noise spectra with ray parameters of 6-9 s/deg. Nevertheless, it's plausible that at least some of the high-velocity noise observed at CMAR is created in this manner.

In Figure 8 we show the correlation of the high-velocity noise time series with ocean wave heights for distances less than 90° from CMAR, which is equivalent to the hemisphere opposite that shown in Figure 7. The seemingly strong correlation in the Barents Sea is an artifact related to the extrapolation of our ocean height model to latitudes above what is covered by TOPEX/POSEIDON satellite tracks; however, the strong correlations observed across much of the north Pacific are legitimate. In the bottom panel we compare the seismic noise time series with wave heights from a domain just north of New Guinea, at a distance of around 50° from CMAR. A PcP wave from this area would arrive at CMAR with a ray parameter of 3.7 s/deg from a backazimuth of around 100° . The sample correlation coefficient in this case is 0.37, which is significant above the 99.9% level. Equivalently strong positive correlations are found for regions in the North Pacific near the Aleutians, a region known for large wave heights.

A final possibility is that the high-velocity noise recorded at CMAR is created by direct teleseismic P waves that turn deep in the lower mantle. High correlation with ocean waves in the Pacific is seen for many regions at distances of $60^\circ - 90^\circ$ from CMAR (Figure 8). These P-waves would arrive at CMAR from the east with ray parameters of 4.5-7.0 s/deg, contradicting our observations by about 3-4 s/deg in absolute slowness. But this is the same margin of error as for the PKP interpretation, and so for the reasons mentioned earlier the teleseismic P energy could plausibly contribute to the observed noise.

335 6 Conclusions

336 We calculated frequency-wavenumber spectra for 955 samples of seismic noise
337 recorded at the Chiang Mai seismic array (CMAR) from 1995 through 2004.
338 At frequencies above about 1.4 Hz the noise is isotropic and diffuse. Therefore
339 in array analysis of body waves from small regional events recorded at CMAR,
340 the assumption of an isotropic noise model is justified and gains close to $\sqrt{18}$
341 are expected when processing high-passed waveforms with coherent signals.

342 At frequencies lower than 1.4 Hz the noise at CMAR is strongly partitioned by
343 apparent velocity into two categories: teleseismic P wave energy with apparent
344 velocities higher than 25 km/s (ray parameters of 0.0-5.0 s/deg) and higher
345 mode Rayleigh energy with apparent velocities near 4.0 km/s. The ring of
346 slowness space in between, corresponding to P waves turning in the crust and
347 upper mantle, is relatively quiet. The Rayleigh noise is further partitioned
348 by direction, with the strongest signal arriving from the Bay of Bengal at
349 backazimuths of $180^\circ - 255^\circ$. A secondary peak in the Rayleigh noise occurs
350 in the direction of the South China Sea at backazimuths of $80^\circ - 120^\circ$. Little
351 noise arrives from the north, the direction of the main Asian landmass and
352 the nuclear test sites of India, Pakistan, China, and North Korea.

353 The Rayleigh noise is strongly seasonal with annual variations of 10-15 dB
354 in power. The easterly noise has peaks in local winter and troughs in lo-
355 cal summer, while the noise from the southwest has the opposite pattern.
356 This behavior is well-matched by the seasonal anti-correlation in significant
357 wave heights in the South China Sea and the Bay of Bengal, as determined
358 from TOPEX/POSEIDON satellite tracks. For a magnitude scale such as

359 MS(Vmax) (Russell, 2006; Bonner et al., 2006) that depends directly on the
360 logarithm of seismic amplitude, our observations imply that the detection
361 threshold at CMAR varies by 0.5-0.75 magnitude units according to direction
362 and time of year.

363 While propagating Rayleigh waves are often observed in seismic noise, it is
364 less common to observe teleseismic body waves. Nearly all reports of body
365 wave noise document ray parameters of 8-12 s/deg, which correspond to P
366 waves that turn in the upper mantle (e.g., Toksoz & Lacos, 1968; Haubrich
367 & McCamy, 1969; Cole et al., 1989; Gerstoft et al., 2006). Therefore, our
368 observations of a consistent noise peak with ray parameters of 4.5 s/deg and
369 smaller, equivalent to apparent velocities of 25 km/s and higher, may be unique
370 in the geophysical literature.

371 Like the Rayleigh noise, the P noise observed at CMAR is seasonal. It has
372 an annual power variation of 5-10 dB, with peaks in local winter and troughs
373 in local summer. The seasonality implies that the noise is unrelated to small
374 unidentified earthquakes or other tectonic processes, and instead is created
375 at least indirectly by ocean waves, similar to the Rayleigh noise. Under this
376 assumption there are several geographical regions that could act as sources:
377 the western Atlantic Ocean near the coast of northern Brazil may contribute
378 PKP energy, the Pacific Ocean just north of New Guinea may contribute PcP
379 energy, and central portions of the North Pacific may contribute P waves that
380 turn in the lower mantle. However, none of these sources provides an ideal
381 match to our slowness observations and so none are preferred over the others.

382 In order to resolve the uncertainty of the source location of the P noise at
383 CMAR, a finer comparison of seismic data and ocean wave data is required.

384 Ideally, we would compare daily or even hourly samples of seismic noise to
385 the geographical tracks of named storms and/or to equally uniformly sampled
386 ocean wave height data from buoys. Observations of P noise from other arrays
387 in the general area would also help, especially if those arrays are slightly wider
388 aperture than CMAR with correspondingly smaller slowness biases related to
389 near-receiver heterogeneity. In any case, and irrespective of the precise source
390 mechanism for the high velocity noise, our observations point towards a new
391 method of imaging Earth's deep interior. Just as Rayleigh microseismic noise
392 has been used to image Earth's crust (Shapiro et al., 2005) it may be possible
393 to use microseismic P-noise to image Earth's lowermost mantle and core.

394 Data and Resources. The TOPEX/POSEIDON Significant Wave Height
395 data were obtained from the Physical Oceanography Distributed Active Archive
396 Center (PO.DAAC) at the NASA Jet Propulsion Laboratory, Pasadena, CA.
397 They are publically available. Seismograms used in this study were obtained
398 from U.S. National Data Center (NDC) maintained by the Air Force Technical
399 Applications Center (AFTAC) in Melbourne, Florida. They are also available
400 to the public.

401 Acknowledgements. The work presented here was funded by the U.S. Air
402 Force Research Laboratory under contract FA871806C0003. We are grateful
403 to Dr. P.S. Callahan for assistance in working with the wave height data,
404 and we thank Anton Dainty for critical comments on an earlier version of
405 this manuscript. We used GMT (Wessel & Smith, 1991) to make most of the
406 figures.

References

- Bokelmann, G. H. R., 1995. Azimuth and slowness deviation from the GERES regional array, *Bull. Seismol. Soc. Am.*, **85**, 1456–1463.
- Bondar, I., North, R. G., & Beall, G., 1999. Teleseismic slowness-azimuth station corrections for the international monitoring system seismic network, *Bull. Seismol. Soc. Am.*, **89**, 989–1003.
- Bonner, J. L., Russell, D. R., Harkrider, D. G., Reiter, D. T., & Herrmann, R. B., 2006. Development of a time-domain, variable-period surface-wave magnitude measurement procedure for application at regional and teleseismic distances, part II: Application and Ms-*mb* performance, *Bull. Seismol. Soc. Am.*, **96**, 678–696.
- Bungum, H., Rygg, E., & Bruland, L., 1971. Short-period seismic noise structure at the Norwegian seismic array, *Bull. Seismol. Soc. Am.*, **61**, 357–373.
- Burg, J., 1964. Three-dimensional filtering with an array of seismometers, *Geophysics*, **39**, 693–713.
- Callahan, P. S., Morris, C. S., & Hsiao, S. V., 1994. Comparison of TOPEX/POSEIDON σ_0 and significant wave height distributions to Gecosat, *Journal Geophysical Research*, **99**, 25015–25024.
- Capon, J., 1969. High-resolution frequency-wavenumber spectrum analysis, *Proc. IEEE*, **57**, 1408–1418.
- Cessaro, R. K., 1994. Sources of primary and secondary microseisms, *Bull. Seismol. Soc. Am.*, **84**, 142–148.
- Cole, S., Claerbout, J., Nichols, D., & Zhang, L., 1989. Ambient seismic field in three dimensions, in *59th Annual Internat. Mtg., Soc. Expl. Geophys.*, p. 395, Soc. Expl. Geophys.
- Douglas, A., 1998. Making the most of the recordings from short-period seis-

433 monometer arrays, *Bull. Seismol. Soc. Am.*, 88, 1155–1170.

434 Engdahl, E. R. & Felix, C., 1971. Nature of travel time anomalies at LASA,
435 *J. Geophys. Res.*, 76, 2706–2715.

436 Gerstoft, P., Fehler, M. C., & Sabra, K. G., 2006. When Katrina hit California,
437 *Geophys. Res. Lett.*, 33, L17308, doi:10.1029/2006GL027270.

438 Haubrich, R. A., 1968. Array design, *Bull. Seismol. Soc. Am.*, 58, 977–991.

439 Haubrich, R. A. & McCamy, K., 1969. Microseismic: Coastal and pelagic
440 sources, *Rev. Geophys.*, 7, 539–571.

441 Ingate, S. F., Husebye, E. S., & Christofferson, A., 1985. Regional arrays and
442 optimum data processing schemes, *Bull. Seismol. Soc. Am.*, 75, 1155–1177.

443 Koper, K. D., Franks, J., & Dombrovskaya, M., 2004. Evidence for small-scale
444 heterogeneity in Earth’s inner core from a global study of PKiKP coda
445 waves, *Earth Planet. Sci. Lett.*, 228, 227–241.

446 Lacos, R. T., Kelly, E., & Toksóz, M. N., 1969. Estimation of seismic noise
447 structure using arrays, *Geophysics*, 34, 21–38.

448 Longuet-Higgins, M., 1950. A theory of the origin of microseisms, *Phil. Trans.*
449 *Roc. Soc. Lon. A*, 243, 1–35.

450 Louie, J., 2001. Faster, better: Shear-wave velocity to 100 meters depth from
451 refraction microtremor arrays, *Bull. Seismol. Soc. Am.*, 91, 347–364.

452 Okada, H., 2003. *The Microtremor Survey Method*, vol. 12 of Geophysical
453 Monograph Series, Society of Exploration Geophysicists, Tulsa, OK.

454 Rhie, J. & Romanowicz, B., 2004. Excitation of Earth’s continuous free oscil-
455 lations by atmosphere-ocean-seafloor, *Nature*, 431, 552–556.

456 Rost, S. & Thomas, T., 2002. Array seismology; methods and applications,
457 *Rev. Geophys.*, 40, doi:10.1029/2000RG000100.

458 Russell, D. R., 2006. Development of a time-domain, variable-period surface-
459 wave magnitude measurement procedure for application at regional and

460 teleseismic distances, part I: Theory, *Bull. Seismol. Soc. Am.*, **96**, 665–677.

461 Schimmel, M. & Paulssen, H., 1997. Noise reduction and detection of weak,
462 coherent signals through phase-weighted stacks, *Geophys. J. Int.*, **130**, 497–
463 505.

464 Schulte-Pelkum, V., Earle, P. S., & Vernon, F. L., 2004. Strong directivity
465 of ocean-generated seismic noise, *Geochem. Geophys. Geosys.*, **5**, Q03004,
466 doi:10.1029/2003GC000520.

467 Schweitzer, J., Fyen, J., Mykkeltveit, S., & Kvaerna, T., 2002. Chapter 9: Seis-
468 mic arrays, in *IASPEI New manual of seismological observatory practice*,
469 edited by P. Bormann, p. 55, GeoForschungsZentrum Potsdam.

470 Shapiro, N. M., Campillo, M., Stehly, L., & Ritzwoller, M. H., 2005. High-
471 resolution surface-wave tomography from ambient seismic noise, *Science*,
472 **307**, 1615–1618.

473 Shumway, R. H., Smart, E., & Clauser, D. A., 2008. Mixed signal processing
474 for regional and teleseismic arrays, *Bull. Seismol. Soc. Am.*, **98**, 36–51.

475 Tibuleac, I. & Herrin, E., 1997. Calibration studies at TXAR, *Seism. Res.*
476 *Lett.*, **68**, 353–365.

477 Toksoz, M. N. & Lacos, R. T., 1968. Microseism: Mode structure and sources,
478 *Science*, **159**, 872–873.

479 Webb, S. C., 1998. Broadband seismology and noise under the ocean, *Reviews*
480 *of Geophysics*, **36**, 105–142.

481 Wessel, P. & Smith, W., 1991. Free software helps map and display data, *Eos*
482 *Trans. AGU*, **72**, 441, 445–446.

Figure Captions

Figure 1. (left) Location and geometry of the Chiang Mai seismic array (CMAR). The dark triangle is the reference point for the array. (right) The array response function for a vertically incident 1 Hz plane wave. Note that the sidelobes are distant and weak. At lower frequencies, the sidelobes are even further separated from the main-lobe in slowness space.

Figure 2. Frequency-wavenumber spectra for a time window starting of seismic noise starting at approximately 08:30:00 GMT on March 26, 1996. The panels on the left show results from the frequency domain technique for a 160 s time window, and the panels on the right show results from the time domain technique for a 64 s subwindow. Frequency increases from top to bottom in both cases. The inner ring indicates a ray parameter of 4.4 s/deg (phase velocity of about 25 km/s), the middle ring indicates a ray parameter of 27.8 s/deg (phase velocity of 4 km/s), and the outermost ring indicates a ray parameter of 40.0 s/deg (phase velocity of about 2.8 km/s). Therefore, energy arriving within the inner ring possesses a ray parameter smaller than P_{diff} , and so has likely interacted with Earth's core. Energy arriving between the two outer rings is consistent with higher-mode Rayleigh waves, and is typical of short-period noise recorded at arrays.

Figure 3. Stacked frequency wavenumber spectra for the 955 time windows. Subpanels are the same as described in Figure 2.

Figure 4. Histograms of peak noise power for the 955 time windows. The global maxima were selected from the time-domain algorithm applied in the 0.33-0.67 Hz band. We show the full 2D histogram in 0.5 s/deg by 0.5 s/deg bins with circles drawn at apparent velocities of 25 km/s, 4 km/s, and 2.8 km/s for the (a) raw and (b) corrected slownesses. The corresponding ray parameter histogram in bins of 1 s/deg are shown in panels (c) raw and (d) corrected.

Figure 5. Correlation of the Pacific Ocean Rayleigh wave microseismic energy with ocean wave heights. In the top panel the seismically constrained source area is shown by the wedge shape, and the color indicates the correlation coefficient between the seismic noise and the significant ocean wave heights. The time dependence of the seismic noise is shown by the black curve in the bottom panel, and the red curve represents significant wave height for a domain of 11°N-15°N and 111°E-115°E.

Figure 6. Correlation of the Indian Ocean Rayleigh wave microseismic energy with ocean wave heights. In the top panel the seismically constrained source area is shown by the wedge shape, and the color indicates the correlation coefficient between the seismic noise and the significant ocean wave heights. The time dependence of the seismic noise is shown by the black curve in the bottom panel, and the red curve represents significant wave height for a domain of 8°N-12°N and 91°E-95°E.

Figure 7. Correlation of the high-velocity microseismic energy with ocean wave heights, assuming a PKP source. In the top panel the seismically con-

533 strained source area is shown by the annulus, and the color indicates the cor-
 534 relation coefficient between the seismic noise and the significant ocean wave
 535 heights. The time dependence of the seismic noise is shown by the black curve
 536 in the bottom panel, and the red curve represents significant wave height for
 537 a domain of near the north coast of Brazil defined as 2°S - 3°N and 50°W - 45°W .
 538

539 **Figure 8.** Correlation of the high-velocity microseismic energy with ocean
 540 wave heights, assuming a P/PcP source. In the top panel the circles are drawn
 541 at distances of 30° and 60° from CMAR, and the color indicates the correlation
 542 coefficient between the seismic noise and the significant ocean wave heights.
 543 The time dependence of the seismic noise is shown by the black curve in
 544 the bottom panel, and the red curve represents significant wave height for
 545 a domain just to the north coast of New Guinea defined as 0°N - 10°N and
 546 135°E - 150°E .

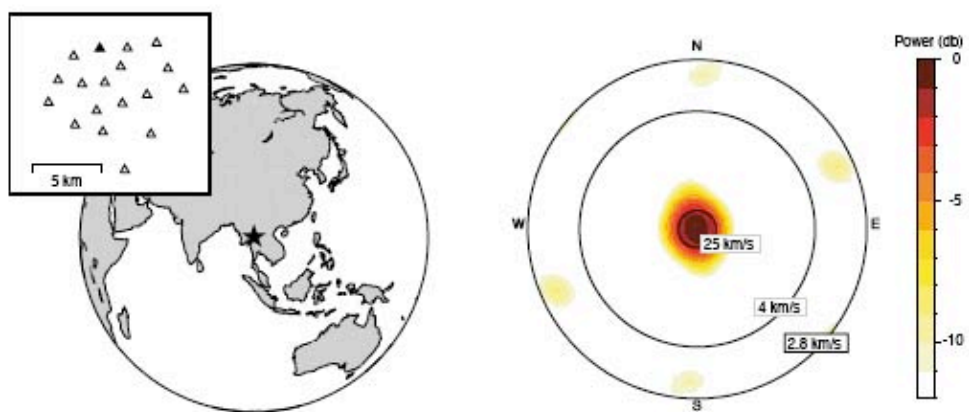


Figure 1

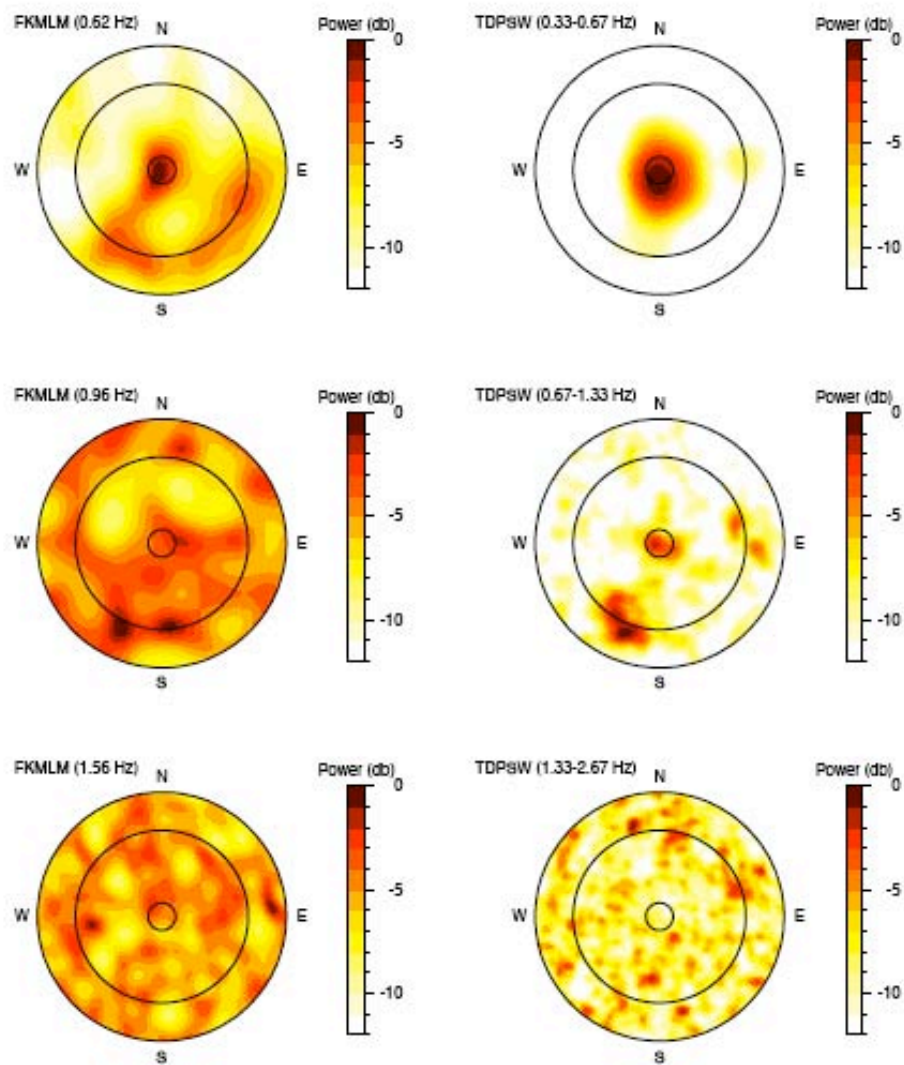


Figure 2

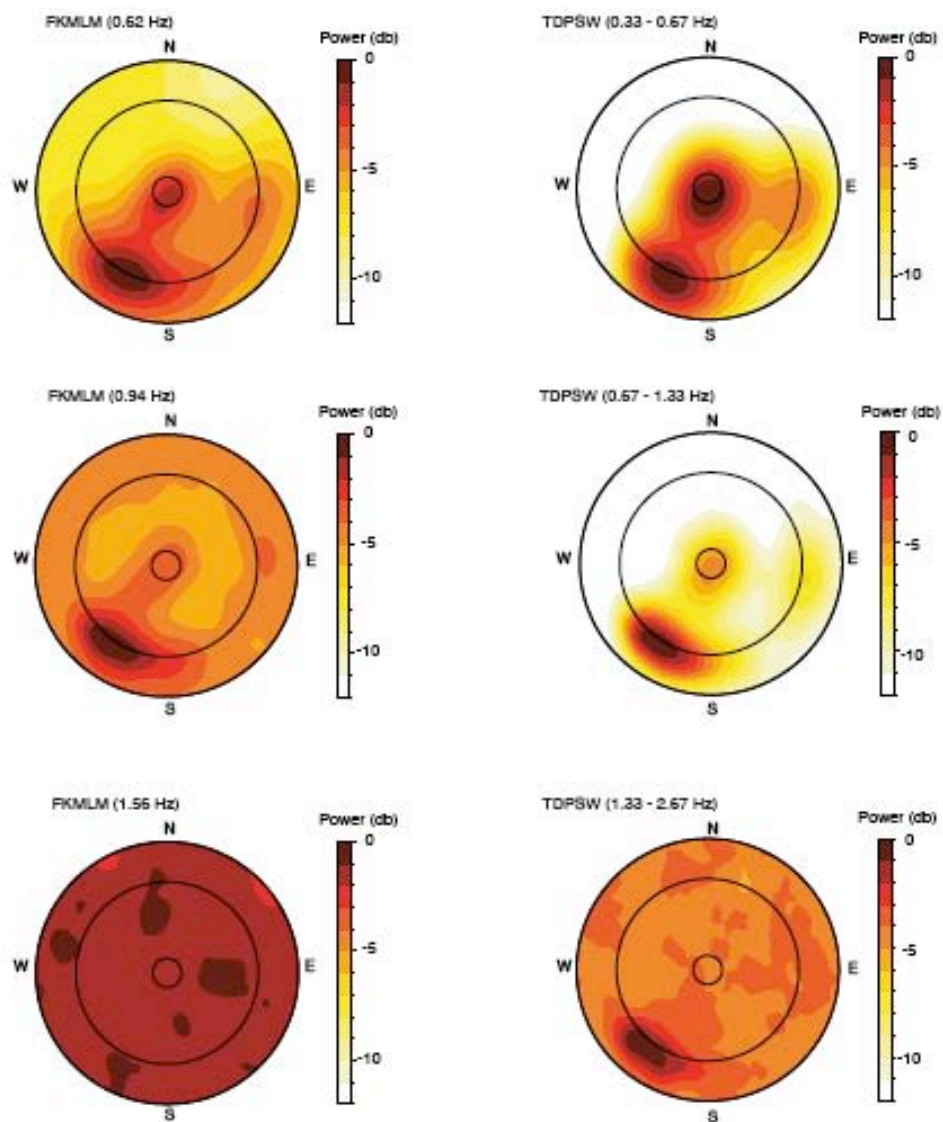


Figure 3

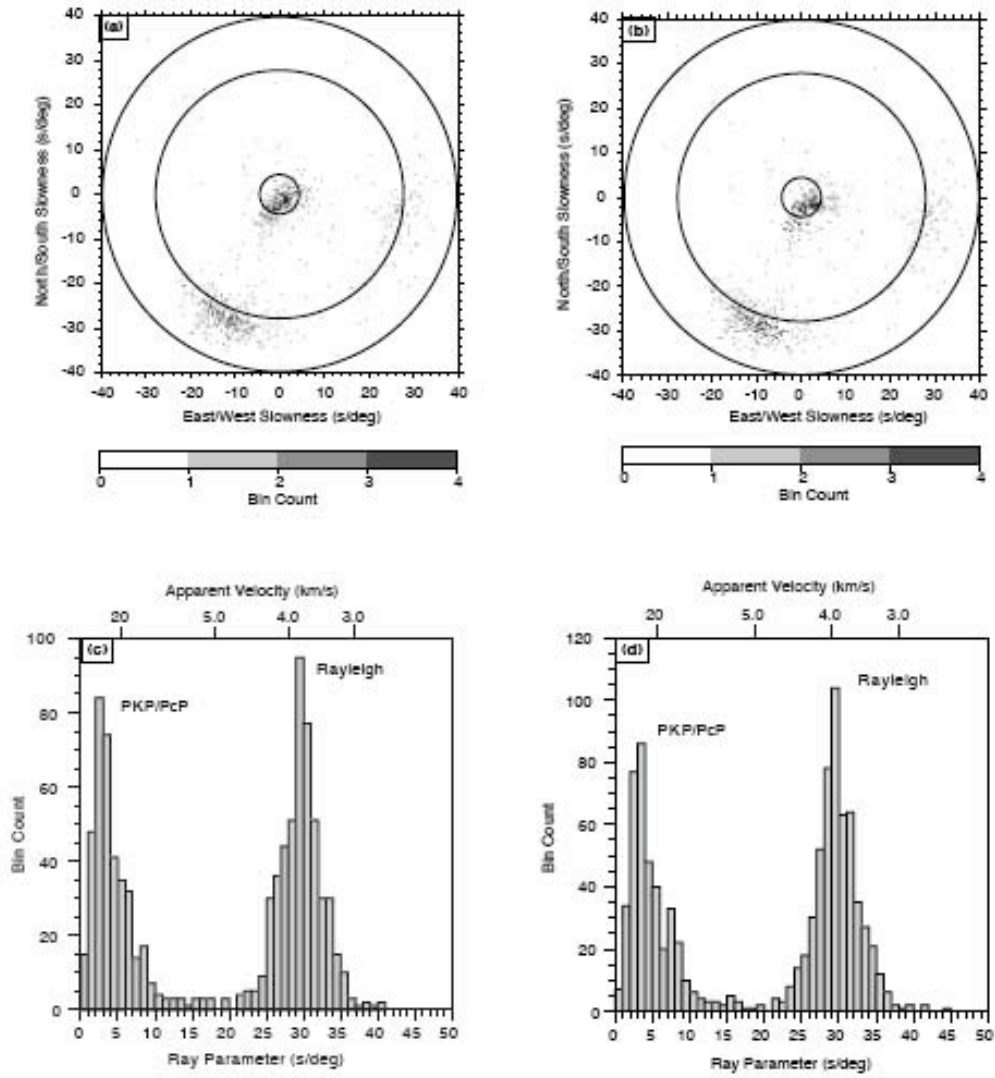


Figure 4

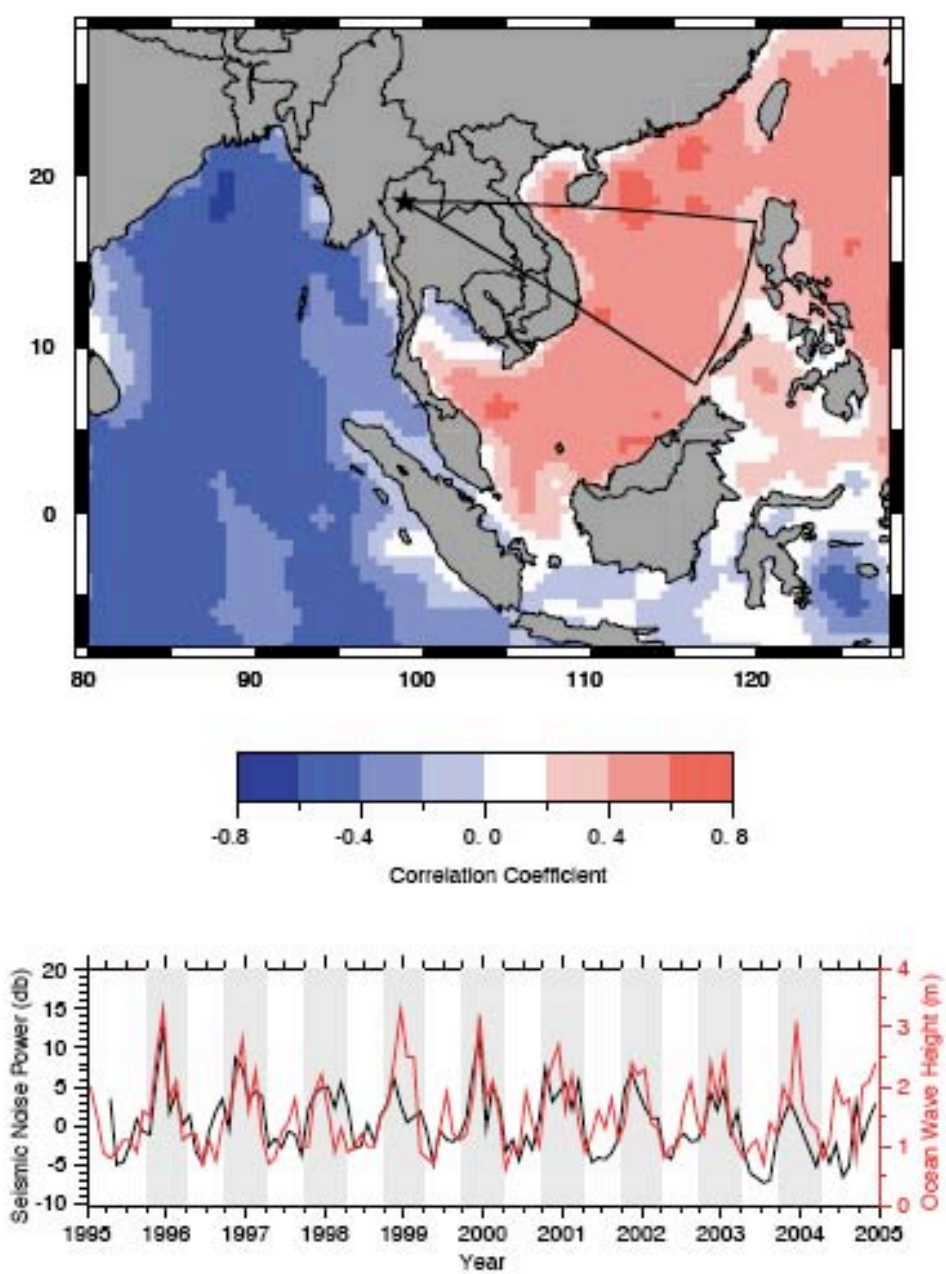


Figure 5

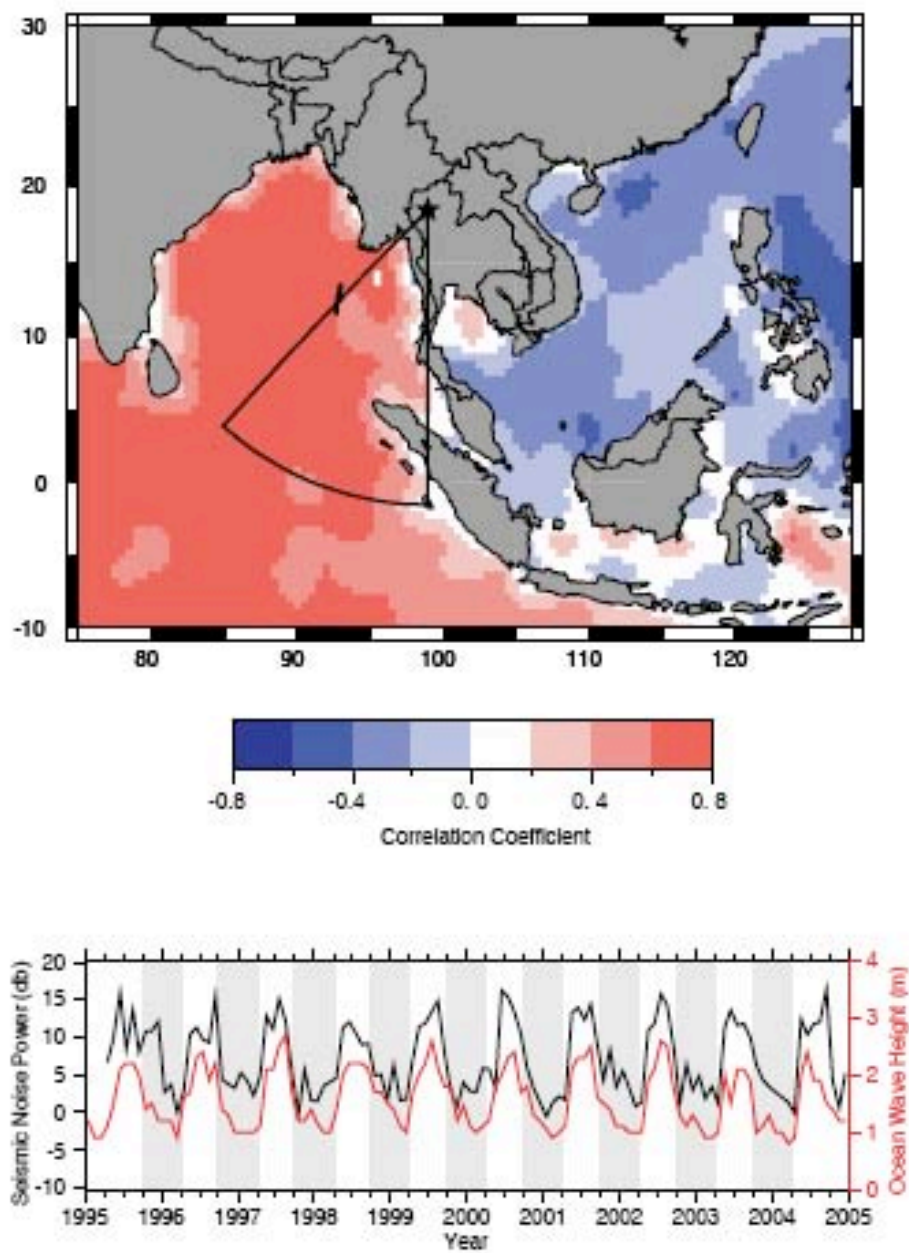


Figure 6

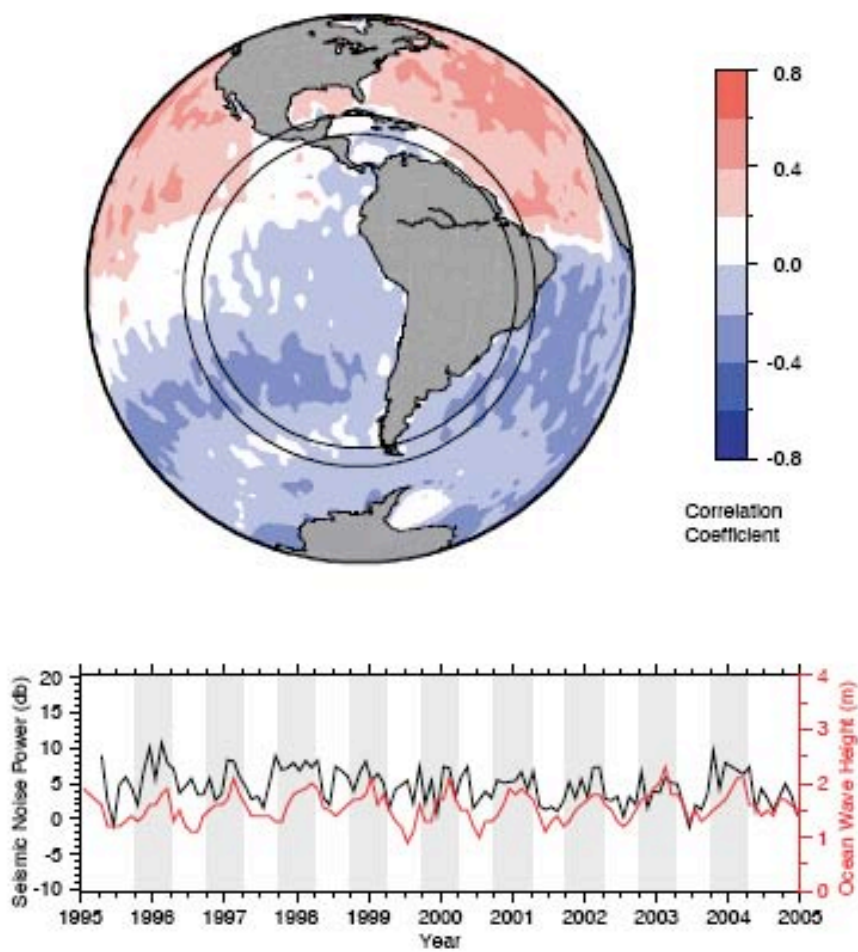


Figure 7

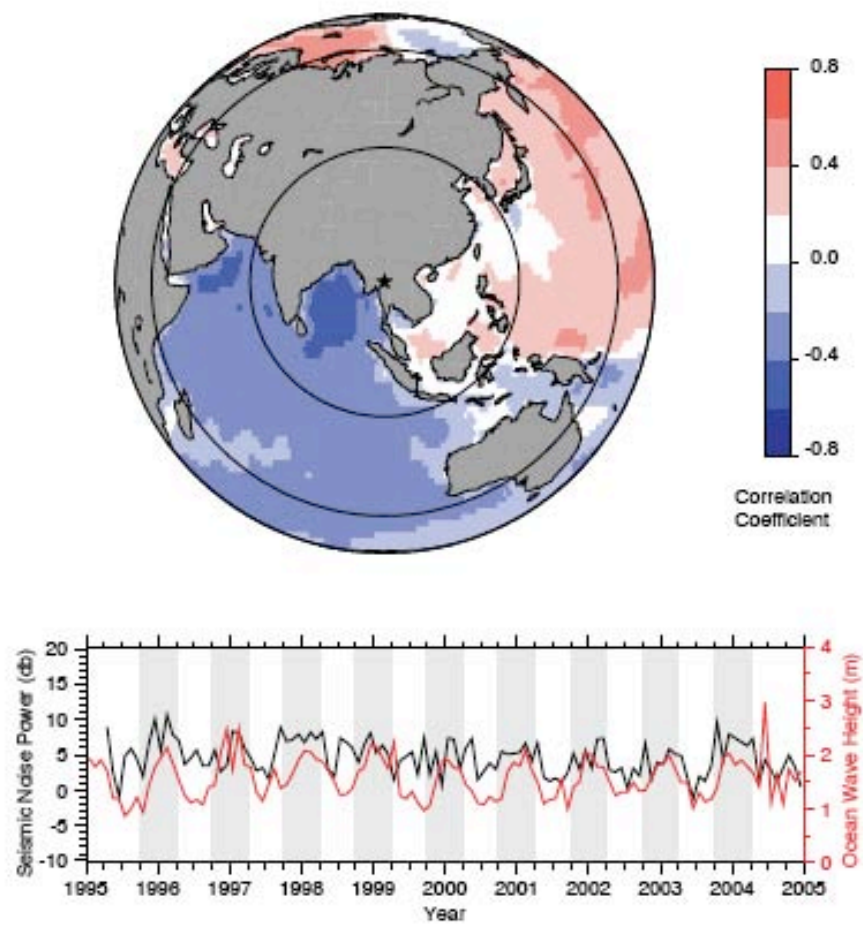


Figure 8

